PROCEEDINGS A

rspa.royalsocietypublishing.org

Review

Article submitted to journal

Subject Areas:
Fluid mechanics, Applied mathematics, Chemical engineering

Keywords:
pressure-driven growth model, foams, front propagation, porous media, Taylor expansion

Author for correspondence:
C. Torres-Ulloa
e-mail:
carlos.torres-ulloa@strath.ac.uk
carlos.torres@uct.cl

THE ROYAL SOCIETY
PUBLISHING

Breakdown of similarity solutions: A perturbation approach for front propagation during foam improved oil recovery

C. Torres-Ulloa[1,2] & P. Grassia[1]

[1]Department of Chemical and Process Engineering, University of Strathclyde, James Weir Building, 75 Montrose St, Glasgow G1 1XJ, UK.
[2] Departamento de Procesos Industriales, Facultad de Ingeniería, Universidad Católica de Temuco, Av. Rudecindo Ortega 02950, Temuco, Chile.

The pressure-driven growth model has been employed to study a propagating foam front in the foam improved oil recovery process. A first order solution of the model proves the existence of a concave corner on the front, which initially migrates downwards at a well defined speed that differs from the speed of front material points. At later times however, it remains unclear how the concave corner moves and interacts with points on the front either side of it, specifically whether material points are extracted from the corner or consumed by it. To address these questions, a second order solution is proposed, perturbing the aforementioned first order solution. However the perturbation is challenging to develop, owing to the nature of the first order solution, which is a similarity solution that exhibits strong spatio-temporal non-uniformities. The second order solution indicates that the corner's vertical velocity component decreases as the front migrates, and that points initially extracted from the front are subsequently consumed by it. Overall, the perturbation approach developed herein demonstrates how early-time similarity solutions exhibiting strong spatio-temporal non-uniformities break down as time proceeds.

1. Introduction

Foam applications occur in several industrial processes,

such as for example: mining, food and cosmetics, production of glass, foam fractionation, firefighting, as well in medicine, in a process known as foam sclerotherapy [1–3]. Specifically, what is studied in the present work, are the applications which involve foam flow through porous media, such as soil remediation and foam improved oil recovery (or foam IOR) [4–6]. In those processes the foam is used to sweep or remove a specific material, be it a pollutant or valuable component from the porous media [7–9]. In petroleum engineering applications, during the oil recovery process, typically up to a third of the oil originally present in the reservoir is recovered, after the primary and secondary stage of extraction [4]. Then, a set of techniques known as enhanced or improved oil recovery can be employed to recover the additional remaining oil from the porous media [5]. In particular, foam IOR is a tertiary oil extraction technique which consists of the injection of gas into the reservoir (see Figure 1), after the deposit has been flooded with a surfactant solution [5]. Upon contacting the surfactant, the gas generates foam, that propagates pushing the liquid (oil and surfactant solution) to the extraction well (see Figure 1). The process relies of course on the foam films that are so formed being stable enough to survive as they propagate through the porous medium, displacing reservoir liquids ahead of them. Stability of propagating foam films in the presence of oil can be challenging, although, surfactant formulations can be found that, for particular oil types, impart good stability to the films [10–14].

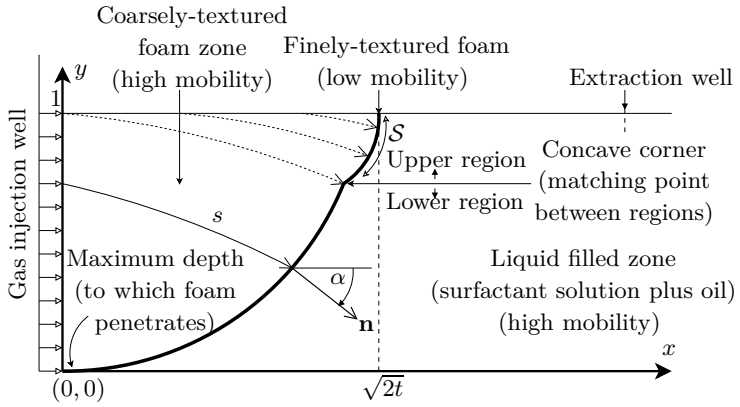

Figure 1: Definition sketch: Foam front propagation across a vertical domain $y \in [0, 1]$ and a horizontal domain $x \in [0, \infty)$. Variables are non-dimensionalised as established in [5,15,16]. Here $\mathcal{S}$ is the distance along the front measured downward. The foam is created by the injection of gas, forming a finely-textured zone of small thickness, at the propagating foam front. The front is represented here by a solid curve, which is vertically divided into two regions, separated by a concave corner, this concave corner being the matching point between an upper and a lower region. Furthermore, the propagation front itself divides the reservoir into two zones: the coarsely-textured foam (to the left) and the liquid filled zone (to the right). Both of these zones have much higher mobility than the propagation front [17,18]. Locally, each point on the front, moves in the normal $\mathbf{n}$ direction, which is measured as an angle α from the horizontal (each point following its own trajectory of length s). The trajectory that has been followed by the points constituting the upper region is drawn with dotted lines, originating at the top boundary, those points having been injected from the top and hence having been part of the front, during less time than the original ones (present from $t = 0$, trajectories drawn with solid line) that constitute the lower region. At the top of the front ($y = 1$) the front position as a function of time is $\sqrt{2t}$ (in dimensionless variables) [15], which will be employed in this work as a top boundary condition.

(a) Foam in porous media

Modelling how this front propagates inside the reservoir is of great interest, since we cannot see what is happening underground. Fortunately there have been numerous studies of the mechanisms by which foam is generated within and propagates within porous media [5,15,19–26], so insights into the elements that are required within a model are available. In porous media, foam films can severely restrict the motion of gas; the gas mobility falls due to the presence of foam films blocking the flow paths of gas [22]. Further upstream where foam is drier, foam films undergo capillary collapse. Upstream then, even though foam films might be present blocking certain pores, if there are sufficient unblocked pores so that gas is able to find a flow path, then mobility is much higher. Hence what restricts motion is the zone of finely-textured foam where injected gas meets liquids [27] already in the reservoir, not drier and coarser foam upstream, nor unfoamed reservoir liquids downstream [17,22]. Therefore, we can track the front propagation by considering just the region where foam is being generated. The thickness of this region, compared to other length scales, i.e. the depth to which the foam penetrates, and the trajectory through which the front has moved, is relatively small, such that it can be considered as a sharp propagation front (a curve with negligible thickness) [15,27]. Hence, the front itself consists of the zone of finely-textured foam, separating (as mentioned above) coarsely-textured, collapsed foam upstream from liquids (surfactant solution and oil) downstream. Foam in porous media is of course a rheologically complex fluid (which amongst other things) can exhibit shear thinning behaviour [19,22,25,28–30]. For the purposes to be considered here though, what matters is that at the front, we have a finely-textured foam which has very low mobility. The total fluid mobility either side of the front is substantially larger than that at the front itself, possibly by as much as four orders of magnitude [17,29], so that it is possible to consider that all the pressure drop occurs across the propagating front, where the entire dynamics is focussed [27]. Consequently, the front is pushed along the reservoir by pressure, and at the same time, is retarded by dissipation across the finely-textured foam zone, the width of this zone gradually increasing with time (as follows from fractional flow theory) but always remaining thin relative to front displacement [15]. As the front motion is driven by the pressure difference across it, its velocity decreases with depth, since the injection pressure behind remains fixed, but the hydrostatic pressure ahead increases with depth. Therefore, there is a maximum depth (used to non-dimensionalise length scales in the system) to which the foam can penetrate, i.e. the depth at which the injected gas pressure equals the hydrostatic pressure [27]. This maximum depth scales proportionally to gas injection pressure and inversely with liquid-gas density difference and gravitational acceleration. Far above this maximum depth however, the front is known to exhibit a concave corner or kink [27] (see Figure 1), which starts off right at the top and migrates downward. Determining how this concave corner moves, is the issue addressed in this work.

(b) Concave corner and spatio-temporal non-uniformities

Physically, the concave corner or kink, corresponds to an abrupt reorientation of the front over a limited length scale. A locally non-smooth front shape, such as this concave corner represents, may induce fingering phenomena, which decrease the process efficiency [15], thereby highlighting the importance of identifying its position. Mathematically, the concave corner arises due to an incompatibility when trying to match material points that have been on the propagation front since the start of the injection process (all found in the so called lower region below the corner) and material points that have been newly injected from the top boundary since the initial time (the so called upper region) [27] (see Figure 2).

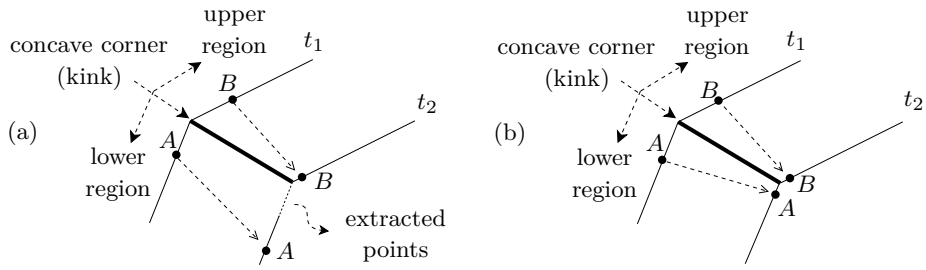

Figure 2: Possible trajectories of material points in the neighbourhood of the kink or concave corner. (a) Points between the fixed material point A and the kink, move away from it, opening a gap between times t_1 and t_2. This gap is filled by points extracted from the kink. Points between the fixed material point B and the kink, are consumed between times t_1 and t_2. (b) An alternative scenario where points between fixed material points A and B, and the kink/corner are consumed over a time interval between t_1 and t_2.

The position of the kink/corner can be tracked over time (see e.g. section 4), in terms of "similarity variables" at early times [27]. Early time here means small compared to characteristic time scale identified in [15] which is used to make the system dimensionless. This time scale turns out to be proportional to the following quantities: gas saturation at the front, porosity of the medium, maximum penetration depth squared, and the (assumed roughly constant, based on fractional flow theory) ratio between front thickness and front displacement, and inversely proportional to medium permeability, relative mobility of foamed gas, and pressure used to drive the foam. A typical value of this time scale has been estimated as around 11–14 days [21,31]. However the important point for the current work is that this time scale is defined such that, at dimensionless time $t = 1/2$, the front has displaced horizontally by an amount equal to its maximum penetration depth [15]. Small time therefore means the top of the front has displaced horizontally by much less than the depth over which the front displaces overall.

Using the similarity solution, a first order approximation to the location of the concave corner or kink was found [27]. However, as time proceeds, the first order similarity solution deviates from a numerical and therefore more exact solution [32]. This first order solution showed the corner moving downwards (at very early times) more slowly than the second order approximation to the material point initially at the top of the lower region, which meant that new material points were being extracted from the kink or corner to populate the lower region (see Figure 2(a)). Nevertheless, given that the second order approximation to the point initially at the top of the lower region indicates that material point's vertical motion slows down over time, eventually it is overtaken by the first order approximation to the corner or kink: material points in the lower region are now being consumed by the kink, not extracted from it (see Figure 2(b)). In this context, extracting material points implies physically that the zone of finely-textured foam would need to thin slightly (at least temporarily), whereas consuming/destroying such points implies that this region must thicken a little (again at least temporarily). These are just temporary effects, since away from the corner, a local balance between microscale foam generation and foam destruction mechanisms quickly restores the thickness of the finely-textured zone to its previous value (i.e. front thickness proportional to front displacement as mentioned above) on time scales much shorter than the total time for which the front propagates [30]. It is not clear however, whether this prediction of material points being extracted/consumed is the actual behaviour or merely an artifact of having a second order approximation for one quantity (the material point) and a first order approximation for the other (the corner). The aim of this paper then is to obtain the second order approximation to the corner or kink location by improving upon the first order solution in the upper region. The question we address then is whether a transition is still seen between the scenario of Figure 2(a) and that of Figure 2(b)

when a consistent second order approximation is used. Obtaining a second order solution in the upper region is however challenging, more so than obtaining second order solutions in the lower region was [27]. Indeed, given that the first order solution is a similarity solution, the generic mathematical challenge we focus on here is exploring how that similarity solution breaks down at second order. Significant spatio-temporal non-uniformities arise in the first order similarity solution for the upper region which are already complicated to handle: a snapshot of the front shape at a fixed very early time will have very sharp curvature, whereas a material point on the front released at very early time will have rapid temporal changes in its vertical velocity component [27]. Hence, we have to perturb the upper region about a solution that evolves over arbitrarily small spatial distances at arbitrarily small times: this then is where the challenge lies.

There is also a question concerning for which set of times a second order solution might be valid given that in [27], although the first order solution was obtained formally for $t \ll 1$, it managed to describe the front shape reasonably well even for values of t up to order unity, as was determined by comparison with numerical results from an Eulerian model [32]. Hence we expect the second order solution should also be valid over a similar time domain. In [32], the shape of a foam front in Eulerian coordinates, was obtained numerically by solving a coupled system of Hamilton–Jacobi equations [33], where the foam front was given implicitly, as the zero-level set [34] of the solution variable. In the Eulerian method it is not necessary to deal explicitly with the aforementioned incompatibility between the positioning of newly injected material points and material points already on the front, since material points are not tracked at all, by contrast with what is required in a Lagrangian method. Nonetheless a concave corner or kink still arises. This kink was then tracked via an Eulerian scheme in [32], and its position at early times was found to be consistent with the Lagrangian estimates from [27]. Nevertheless, numerical artifacts may appear in the Eulerian solution, since we can only ever capture the concave corner to within the numerical grid resolution. This then motivates a return to a Lagrangian approach, to search for an improved analytical approximation which will be free of such artifacts.

(c) Modelling the foam front

We can model the foam front advance through a homogeneous oil reservoir (see Figure 1) by using a dimensionless form of the "pressure-driven growth model", which has been widely studied before [5,15,27,31,35]. The pressure-driven growth model relates the pressure difference across the propagating front to motion, which is in the local normal direction $\mathbf{n} = \hat{\mathbf{i}}\cos(\alpha) - \hat{\mathbf{j}}\sin(\alpha)$, oriented at an angle α below the horizontal (see Figure 1). For the purpose of Lagrangian computation, the propagation front can be discretized into a finite number of material points, the motion of which we can readily track, and the front shape itself at any given time can be reconstructed by following a collection of such points. The dimensionless form of the pressure-driven growth model, developed in [5,15,27,36], and used in this work, establishes that at any local front position $\mathbf{x} = (x, y)$, the motion is governed by,

$$\mathrm{d}\mathbf{x}/\mathrm{d}t = (y/s)\mathbf{n}, \tag{1.1}$$

where $y \in [0, 1]$ represents the distance above the maximum depth (where $y = 0$ represents the bottom and $y = 1$ the top of the solution domain), s is the distance travelled by a material point and $\mathbf{n}$ is the local normal direction. The boundary condition, establishes that at the top ($y = 1$), front position x as a function of time corresponds to $\sqrt{2t}$ [37] in dimensionless form, and at this point the front is completely perpendicular to the top (see Figure 1). A concave corner develops and shifts over time [27] (see Figure 1). This corner is also called a "matching point" since it is where we must match two aforementioned regions that divide the front vertically: the "lower region" incorporating material points originally on the front, and the "upper region" consisting of newly injected points. The upper region starts off being of arbitrarily small extent, but grows over time (the lower region shrinks to compensate). Likewise initially the front reorients by an arbitrarily small angle in the upper region (albeit with arbitrarily large curvature), but the

amount it reorients grows over time (whereas curvature falls). Specifically it was shown by [27] that the upper region is of vertical extent relative to the maximum penetration depth of the front of order t (t here being the dimensionless time) and it reorients through an angle of order $\sqrt{t}$, making curvature become order $1/\sqrt{t}$. As we have said, the concave corner arises as a consequence of an incompatibility between points originally on the front and newly injected points. So, the concave corner itself consists of a point at which material points from either side meet. Both above and below the corner, it is possible to capture analytically for small times $t \ll 1$, how material points move. If we consider according to equation (1.1) that, closer to $y = 1$, the speed of the points is faster, the sign of the $\hat{\mathbf{j}}$ component of the normal $\mathbf{n}$ becomes negative (as in Figure 1), which implies that the points are moving downwards, following

$$\mathrm{d}y/\mathrm{d}t = -(y/s)\,\sin(\alpha), \tag{1.2}$$

as well as moving in the x direction as

$$\mathrm{d}x/\mathrm{d}t = (y/s)\,\cos(\alpha), \tag{1.3}$$

with α being the angle by which $\mathbf{n}$ is oriented below the horizontal. Combined together equations (1.2) and (1.3), give us the evolution of the trajectory path length as

$$\mathrm{d}s/\mathrm{d}t = \sqrt{(\mathrm{d}x/\mathrm{d}t)^2 + (\mathrm{d}y/\mathrm{d}t)^2} = y/s. \tag{1.4}$$

By approximating these equations it is possible to track analytically for small times, the trajectory of the point that was originally at the top ($y = 1$ when $t = 0$). In particular for the vertical coordinate, this can be done at first order (order t) and also at second order (order t^2) (assuming this point has not been consumed by the concave corner) [15,27]. Horizontally this point lags an order $t^{3/2}$ distance behind the top of the front (which is always at location $x = \sqrt{2\,t}$). The trajectory of this material point which was initially at $y = 1$ gives an indication where the concave corner (or kink) may be, but not the exact location, since we are tracking a material point near the concave corner, not the corner itself. As already mentioned, what was found by [15,27] is that the second order correction causes the material point to move down more slowly than the first order approximation predicts. Extending this analysis to material points initially at $y \leq 1$, a solution is obtained for the lower region [27], to be discussed in section 2. In the upper region, front material points are tracked also, but this presents more of a challenge requiring, as previously mentioned, a similarity solution to be developed (see section 3).

To summarise, this work expands upon the methodology used in [27], to obtain a second order accurate solution to track the trajectory of the injected material points for $t \ll 1$, again, in terms of similarity variables in the upper region, but with small perturbations breaking the similarity. This proves challenging to do, because of the strong spatio-temporal non-uniformities associated with the similarity solution. The perturbed solution will be used to find the intersection or matching point between the lower and the upper region of the front (the concave corner or kink), consistently through to second order. The solution will then be interrogated in an effort to establish which scenario (Figure 2(a) or 2(b)) is realised as time progresses, noting that the scenario of Figure 2(a) is necessarily realized at arbitrarily small times. The rest of this work is laid out as follows. In sections 2, 3 and 4 we review the existing methodology derived by [27], the extension to that methodology appearing from section 5 onwards. The second order solution will be expressed, as before, in terms of similarity variables, but admitting small perturbations at small times $t \ll 1$ that break the similarity (see section 5). Then, in sections 6 and 7, using this new solution we will proceed to track the position of the concave corner with an accuracy of second order in time t. Finally, in section 8, we will use the second order solution to compute the shape of the upper region of the front, in comparison with the previous solution given in [27]. Conclusions are offered in section 9.

2. Front propagation in the lower region

This section reviews the theory for the lower region presented in [27]. The key result we derive is equation (2.9), which describes the shape of the lower region. Readers familiar with the derivations from [27] may want to skip directly to section 3.

To determine the front lower region shape, we solve equations (1.2)–(1.4) for $t \ll 1$. For small times the front is close to being a vertical line, the angle α being very small along it. So, we can estimate $\cos(\alpha) \approx 1$, via a leading order Taylor expansion. Moreover, we can also approximate the trajectory as $s \approx x$. Hence, we can compute equation (1.3) as $\mathrm{d}x/\mathrm{d}t \approx y/x$. Then, after integration, we obtain that $x \approx \sqrt{2yt}$, which is known as the Velde solution [15,27]. A higher order solution known as the improved Velde solution was also given in [27], establishing that

$$x \approx \sqrt{2yt + t^2/6}. \tag{2.1}$$

This solution recognises that historically points have been higher up (and hence faster moving) than their current y location indicates. As a result they have moved further than the Velde solution indicates, i.e. the x location computed by equation (2.1) is bigger than $x \approx \sqrt{2yt}$. Up till this point, we have the Velde solution of order $t^{1/2}$ and the improved Velde solution with a correction of order $t^{3/2}$, giving the x displacement of the lower region of the front. We can also obtain an order t solution to compute the vertical location y of the points in the lower region (corresponding to a first order solution). This solution can be derived for small times $t \ll 1$, starting from equation (1.2), with $s \approx \sqrt{2yt}$ and $\sin(\alpha) \approx \alpha \approx \tan(\alpha) \equiv \mathrm{d}x/\mathrm{d}y \approx \sqrt{t/(2y)}$, via the Velde solution. As long as α is small, the curvature of the front $\mathrm{d}\alpha/\mathrm{d}\mathcal{S}$ (with $\mathcal{S}$ being measured down along the front as in Figure 1) can then be approximated by $|\mathrm{d}\alpha/\mathrm{d}y| \approx t^{1/2}y^{-3/2}/(2\sqrt{2})$, so is likewise a small quantity when $t \ll 1$. Using (2.1) in place of the Velde solution only perturbs this curvature slightly. This modest curvature in the lower region is a contrast from the order $1/\sqrt{t}$ curvature that turns out to be present in the upper region. Here we have adopted the notation of [27], where $\mathrm{d}/\mathrm{d}y$ denotes a derivative along a front comprised of various material points at fixed t, whereas $\mathrm{d}/\mathrm{d}t$ denotes a time derivative following a specified material point. Then, integrating equation (1.2), we determine

$$y \approx y_0 - t/2, \tag{2.2}$$

where y_0 is the initial position of a material point originally anywhere below the top $y_0 \leq 1$. Therefore, for the point initially at the top of the lower region ($y_0 = 1$), we can compute

$$y_{1\mathrm{st,lower}} \approx 1 - t/2, \tag{2.3}$$

as its first order approximated location over time. Considering that, at first order, all material points in the lower region migrate downwards with vertical velocity component of $-1/2$, new material points must be injected in order to fill the gap between the $y_0 = 1$ point and the top of the reservoir. Hence, we can define a rescaled form for the vertical coordinate of the points, as

$$\zeta = (1 - y)/(t/2), \tag{2.4}$$

where ζ represents a ratio of distances, that between the top of the reservoir and any arbitrary point y on the front, divided by the vertical distance through which the material point initially at the top of the front has displaced. Here at leading order, ζ takes values from $\zeta = 0$ at the top of the reservoir ($y = 1$), to $\zeta = 1$ for the topmost original material point of the lower region, with $\zeta > 1$ for points even lower down. However, a direct computation of the concave corner (or matching point between the lower and upper regions) found it actually occurs at $\zeta = \zeta_{\mathrm{cross}} < 1$ ($\zeta_{\mathrm{cross}} \approx 0.954$, based on a complex integro-differential equation theory, changing to roughly $\zeta_{\mathrm{cross}} \approx 0.94$ for a simpler but approximate differential equation approach), as shown in [27]. The subscript "cross" denotes the point at which upper and lower regions cross over one another, i.e. the corner or matching point we seek. Since the material point originally at the top of the front is now slightly lower down in y (slightly higher in ζ) than the kink or concave corner is, new material points have been extracted from the kink to fill the lower region (see e.g. Figure 2(a)).

In addition, at any given y, we can define ξ as the horizontal displacement of the front, back from the leading edge at the top of the front $\sqrt{2t}$, given by

$$\xi = \sqrt{2t} - x. \tag{2.5}$$

We can also express ξ geometrically, as

$$\xi = \int_y^1 (\mathrm{d}x/\mathrm{d}y)\,\mathrm{d}y = \int_y^1 \tan(\alpha)\,\mathrm{d}y. \tag{2.6}$$

We cannot yet use equation (2.6) to determine ξ exactly, since it extends all the way into the upper region, for which α versus y is still unspecified. However, we can still use it to estimate the order of magnitude of ξ, under the assumption that α (albeit not curvature approximated here by $|\mathrm{d}\alpha/\mathrm{d}y|$) has similar order of magnitude moving between the upper and lower regions. For small times $t \ll 1$, since $\alpha \approx \sqrt{t/(2y)}$ via the Velde solution (with $\alpha = \mathrm{atan}(\mathrm{d}x/\mathrm{d}y) \approx \mathrm{d}x/\mathrm{d}y$), we define Ξ as, the rescaled in time horizontal displacement [27], via

$$\Xi = \xi/t^{3/2}, \tag{2.7}$$

which recognises that ξ is an order $t^{3/2}$ quantity, since we are integrating an order $\sqrt{t}$ quantity over an order t distance in the y direction close to $y = 1$ (see equation (2.4)). Furthermore, we can express the lower region of the front, corresponding to $\zeta \geq \zeta_{\mathrm{cross}}$, in terms of ζ and Ξ, by first substituting equation (2.1) into equation (2.5), to obtain

$$\xi = (2t - x^2)/(\sqrt{2t} + x) \approx (2t - 2yt - t^2/6)/(\sqrt{2t} + x), \tag{2.8}$$

and then specifically near the top of the domain where $x \approx \sqrt{2t}$, we can obtain after introducing equations (2.4) and (2.7), that

$$\Xi \approx (\zeta - 1/6)/(2\sqrt{2}), \quad \text{if} \quad \zeta \geq \zeta_{\mathrm{cross}}, \tag{2.9}$$

where, $\zeta \geq \zeta_{\mathrm{cross}}$ here requires

$$y \leq y_{\mathrm{cross}} \equiv 1 - (t/2)\zeta_{\mathrm{cross}}, \tag{2.10}$$

which implies that (2.9) is a solution describing specifically the lower region up to the matching point or concave corner at location y_{cross} as defined by equation (2.10). The utility of equation (2.9) is that it gives a Ξ versus ζ relation for the lower region, and if we can also obtain a Ξ versus ζ relation for the upper region, we can find where the two regions intersect, and hence determine ζ_{cross}. This is what [27] achieved, by expressing the upper region in terms of a similarity equation (see section 3 and also, in supplementary material, section S 1 along with section S 2). Note that equation (2.9) is a leading order solution for Ξ, accurate to order $t^{3/2}$. Later on in section 5, we introduce equation (5.4), which corresponds to an order $t^{5/2}$ accurate solution for the lower region, close to the concave corner, improving upon equations (2.1) and (2.9) (see also details in supplementary material section S 3).

Geometrically, equation (2.1) is a parabola, and (2.9) represents a tangent to that parabola at $y = 1 - t/2$ or equivalently at $\zeta = 1$, the geometrical distance between the parabola and its tangent being negligible at the current order of approximation. Having this approximation for the front lower region, it is possible to obtain a more accurate (second order) estimate of the trajectory y as a function of time t for material points in the lower region, as an improvement over and above equation (2.2). As was proven in [27], such points move obeying

$$y \approx y_0 - t/2 + 5\,t^2/(48\,y_0), \tag{2.11}$$

where $y_0 \leq 1$ is initial location of the points when $t = 0$. Equation (2.11) is a perturbation of (2.2) indicating that when $t \ll 1$ all points move downwards with the same leading order velocity, and moreover velocity changes away from this leading order value only gradually with time. So, assuming that the $y_0 = 1$ point (the point originally at the top of the front), has not been consumed yet by the concave corner, so its location can still be tracked, and assuming it remains reasonably close to the concave corner itself (to the extent that the aforementioned

value of $\zeta_{\text{cross}} \approx 0.94$, is relatively close to unity), we have an indication of where the junction between the upper and the lower region might be using equation (2.11). Indeed, we can compute the approximate vertical location of the topmost original material point in the lower region as

$$y_{\text{2nd,lower}} \approx 1 - t/2 + 5\,t^2/48 \approx 1 - 0.5\,t + 0.1042\,t^2. \tag{2.12}$$

In summary, we have a first order estimate of the kink location y_{cross}, given by equation (2.10), and a second order estimate $y_{\text{2nd,lower}}$ (equation (2.11)) for a material point that improves upon equation (2.3) and that we postulate, is close to the kink location, although without definitive proof. The reason that the estimate $y_{\text{2nd,lower}}$ was so readily obtained is that the lower region is comparatively uniform in space and time when $t \ll 1$, i.e. low curvatures of the front and weak perturbations away from a leading order material point velocity. Our objective now is to obtain a second order correction to the equation for y_{cross}. Before achieving that however we need to switch over focus to the upper region. As we will see, analysing the upper region proves to be challenging due to strong spatio-temporal non-uniformities that are present there.

3. First order location of the upper region's material points

In this section we review the methodology employed in [27], to determine the first order solution for the shape of the upper region of the front, in order to determine how it might match with the lower region. The key results we derive are equations (3.3)–(3.5), which describe the shape of the upper region of the front, parametrically, in terms of a parameter ψ, which represents the fraction of time that an injected point has been on the front. We start by introducing similarity equations in the upper region, and then based on these, we develop an order time t solution to compute the vertical y movement of the points of the front's upper region, along with an order $t^{3/2}$ expression for the x displacement. Readers familiar with the derivations from [27], may prefer to skip directly to section 4. Higher order corrections are considered later on in section 5.

(a) Introducing similarity variables

As [27] showed, if at any given small instant in time ($t \ll 1$), the location and orientation of a material element (treated as a set of closely spaced collinear material points) is identified relative to the overall extent of the upper region and overall amount that the upper region reorients (both of which happen to be arbitrarily small when $t \ll 1$), then it should be possible to collapse together the front shapes in the upper region at different instants of time into a self-similar form. Hence, we can express the front orientation angle α of the upper region, as

$$\alpha = \sqrt{t/2}\,A(\zeta), \tag{3.1}$$

where A is a function of the variable ζ defined earlier [27] (see also section S 1 in supplementary material, which specifies the function implicitly as $\zeta = \zeta(A)$). If t is small here, α is likewise small. On the other hand, using (2.4) and (3.1), curvature $\mathrm{d}\alpha/\mathrm{d}\mathcal{S}$ which is approximately $|\mathrm{d}\alpha/\mathrm{d}y|$ becomes $(t/2)^{-1/2}\,\mathrm{d}A/\mathrm{d}\zeta$, and hence is large when t is small. Note also that $\sqrt{t/2}$ is, at leading order, the amount that a material element reorients at the top of the lower region. This leading order estimate is obtained via the Velde solution, since we are looking at small times $t \ll 1$ close to $y \approx 1$. Knowing the top of the lower region reorients to $\alpha \approx \sqrt{t/2}$, if we compare this with equation (3.1) for the upper region, any value of $A(\zeta)$ greater than unity at the bottom of the upper region thereby implies a concave kink. Moreover, the front meets the top perpendicularly, as the boundary condition at $y = 1$ requires that the angle $\alpha = 0$ there. This then implies that A varies from 0 at the top, to some value A_{cross} at the cross-over or matching point, estimated to be at $\zeta = \zeta_{\text{cross}}$. We know from [27], that ζ_{cross} is slightly less than unity, so at leading order, the kink or concave corner moves down slightly more slowly than material points originally at the top of the lower region. Moreover [27] showed that $A_{\text{cross}} \approx 1.18$ roughly, which is slightly greater than unity, so the upper region reorients more than the lower region does. As mentioned earlier, that is what produces the kink or corner.

(b) First order upper region representation in terms of ψ

Since points originally on the front $y_0 \leq 1$ move downward (as we demonstrated in section 2), material points must be injected from the top onto the front [15], in order to have a continuous solution over time. For the upper region, we define t_{inj}, as the time at which a material point has been injected. For a fixed time t, we require that $t_{\text{inj}} \in (0, t]$. As in [27], we can define a coordinate ψ such that $1-\psi$ is the ratio between t_{inj} and t, as

$$\psi = 1 - t_{\text{inj}}/t. \tag{3.2}$$

We can express the front location (coordinates ζ and Ξ) in terms of ψ instead of A (contrast section S 1 in supplementary material). Here ψ can be varied by fixing t and varying t_{inj} (thereby looking at a collection of different material points) or alternatively by fixing t_{inj} and varying t (following the trajectory of an individual material point): both ways of varying ψ turn out to be useful later on. If t_{inj} is significantly smaller than t, the points injected tend to be already close to the concave corner, implying that $\psi \to \psi_{\text{cross}}$. Here, $\psi_{\text{cross}} < 1$ (via the integro-differential theory, typically $\psi_{\text{cross}} \approx 0.948$ [27]; or alternatively $\psi_{\text{cross}} \approx 0.9431$ for the simpler differential equation approach to be employed here, see section 7.4.3 in [27]), corresponds to the maximum value of ψ, which is reached at the concave corner. Points with t_{inj} smaller than $(1-\psi_{\text{cross}})t$ have already been consumed by the concave corner, so are no longer part of the propagating front (see Figure 2). By contrast, if $t_{\text{inj}} \to t$, the material points are near to the top, which implies that $\zeta \ll 1$, $A \ll 1$, $\Xi \ll 1$ and $\psi \ll 1$. To date, we have presented a first order theory of the upper region as per [27]. The second order theory to be presented from section 5 onwards, is most naturally expressed in terms of the variable ψ defined by equation (3.2), rather than in terms of A as is presented in section S 1 in supplementary material. Before tackling the second order theory therefore, we need to recast the theory for the upper region in terms of ψ, and then explain how to identify the matching point between the lower and upper region.

As mentioned previously, at small times $t \ll 1$, we can collapse together the front shapes at different times, expressing the shape in terms of similarity variables A, ζ and Ξ, instead of α, y and ξ. In particular, assuming that the upper region of the front consists of a set of material points, each one injected at a different time $t_{\text{inj}} \in (0, t]$, we can compute the front shape for a fixed time t in terms of ψ, varying it between 0 up to some ψ_{cross}. It follows from [27] that

$$A \approx A_0 \equiv (1-(1-\psi)^c)/c, \tag{3.3}$$

where $2c-1$ is the assumed invariant ratio between $\mathrm{d}s/\mathrm{d}y$ and $\mathrm{d}x/\mathrm{d}y$, over the upper region [27] (see section S 1 in the supplementary material). Substituting into equation (S 1.2) we deduce that

$$\zeta \approx \zeta_0 \equiv (1 - c\psi - (1-\psi)^c)/(c(1-c)). \tag{3.4}$$

Equations (3.3)–(3.4) have been expressed in the form $A_0(\psi)$ and $\zeta_0(\psi)$ to highlight that they are leading order expressions which may need to be corrected as time increases. It can be readily checked that $\mathrm{d}\zeta/\mathrm{d}A \equiv (\mathrm{d}\zeta/\mathrm{d}\psi)/(\mathrm{d}A/\mathrm{d}\psi)$, when computed at leading order via equations (3.3)–(3.4), is compatible with equation (S 1.1) (the original form given by [27]). We also obtain a leading order expression for the rescaled horizontal displacement of the upper region $\Xi = (2\sqrt{2})^{-1}\int_0^\zeta A\,\mathrm{d}\zeta$ in the form $\Xi \approx \Xi_0(\psi)$, by substituting from equations (3.3)–(3.4) to give

$$\Xi \approx \Xi_0 \equiv \frac{2c((1-\psi)^c - c - 1)\psi + (1+c)(1-\psi)^{2c} - 2(2c+1)(1-\psi)^c + 3c + 1}{4\sqrt{2}c^2(1-c^2)}. \tag{3.5}$$

Taken together (3.4) and (3.5), both in terms of ψ, give a parametric representation of the upper region of the front, with the same order of accuracy in time as the lower region as computed by equation (2.9), i.e. order $t^{3/2}$ in ξ and order t in y. Therefore, we can determine in terms of ψ, the matching point between the lower and the upper region of the front. This is how [27] proceeded to obtain ψ_{cross}, and the details will be discussed in the next section.

4. First order matching point between upper and lower region

Now we review the methodology used in [27] to determine the first order vertical location of the concave corner over time. Reviewing this enables us subsequently to extend that methodology to second order in section 5. The key first order results are shown in Figure 3. A snapshot of the shape of the front is plotted in Figure 3(a), and in Figure 3(b), the trajectory of the concave corner at leading order is plotted, in comparison with the first order approximated trajectory of material points in the upper and lower region. Having consulted Figures 3(a)–(b), some readers may prefer to skip to section 5, in which the methodology is extended to higher order solutions.

Our immediate objective via Figure 3, is to obtain the first order matching point between the lower and upper region of the front (namely the concave corner). We proceed by plotting both regions, using equation (2.9) for the lower region, and equations (3.4)–(3.5) for the upper region, identifying the intersection or matching point (see Figure 3(a)). Assuming $c = 3/4$ (the value given by [27], see supplementary material section S 1 for details), the matching point between these two regions turns out to be $\zeta_{\rm cross} \approx 0.9397$ and $\Xi_{\rm cross} \approx 0.2733$, and is obtained at $\psi_{\rm cross} \approx 0.9431$ (see Figure 3(a)). This same result was previously obtained in [27] albeit expressed not in terms of ψ but rather in terms of A (equations (S 1.2)–(S 1.3)), with the corner found at $A_{\rm cross} \approx 1.18$ roughly. Given the value of $\zeta_{\rm cross}$, we can compute via equation (2.10)

$$y_{\rm 1st,cross} = 1 - 0.4698\, t, \tag{4.1}$$

as the first order vertical location of the concave corner (the cross-over or matching point between the upper and the lower region of the front). Here we employ the notation $y_{\rm 1st,cross}$ (instead of simply $y_{\rm cross}$ used earlier) to emphasise that this is a first order solution. In the rest of the section we explore some consequences and concepts that follow from having found the first order matching point. These will be generalized to second order in later sections of the paper.

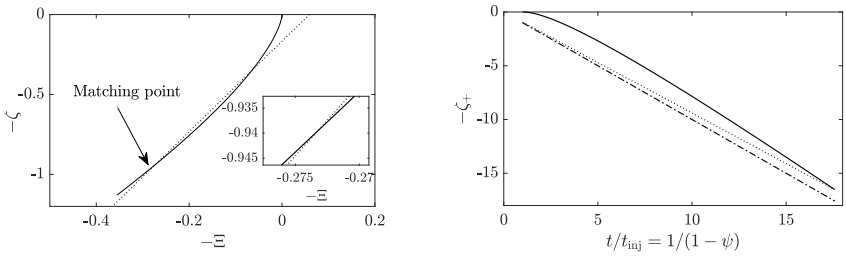

Figure 3: (a) Matching point between the lower (dotted line) and the upper (solid line) region of the front. Here, $-\zeta$ is the rescaled vertical y location of the front and $-\Xi$ is the rescaled horizontal displacement of the front behind the leading edge at the top. We decide to plot $-\Xi$ vs $-\zeta$, since it has the same orientation as x versus y. We obtain that the matching point occurs at $\psi_{\rm cross} \approx 0.9431$. Here, $\zeta_{\rm cross} \approx 0.9397$ and $\Xi_{\rm cross} \approx 0.2733$. (b) Rescaled $-\zeta_+(\psi)$ location (see supplementary material section S 2 for additional details) versus a rescaled time defined as $t/t_{\rm inj} = 1/(1-\psi)$ with $0 \le \psi \le \psi_{\rm cross} \approx 0.9431$. Solid curve represents the trajectory $-\zeta_+$ of a material point moving through the upper region as $-\zeta(\psi)/(1-\psi)$, with $\zeta(\psi) \equiv \zeta_0(\psi)$ at leading order as given by equation (3.4). Note this is not a straight line, implying non-uniform motion. Dotted line shows the $-\zeta_+$ position of the concave corner itself, namely $-\zeta_{\rm cross}/(1-\psi)$, with $\zeta_{\rm cross} \approx 0.9397$. The solid curve and the dotted line coincide only when $\psi = \psi_{\rm cross} \approx 0.9431$. Dash-dotted line shows the trajectory in terms of $-\zeta_+$ of a point in the lower region that was originally at the top of the front, as $-1/(1-\psi)$.

Further details can be found in supplementary material section S 2 which based on the value of ψ_{cross} defines $t_{\text{inj(min)}}(t)$ (the earliest injected point still surviving on the front at time t) and $t_{\max}(t_{\text{inj}})$ (the maximum time out to which a point injected at t_{inj} survives). Supplementary material section S 2 also presents another rescaling of the y coordinate $\zeta_+ = (1-y)/(t_{\text{inj}}/2) = \zeta/(1-\psi)$ which is relevant to Figure 3(b). Whilst the variable ζ is useful for representing the shape of the front at fixed t, the variable ζ_+ is more useful for representing the trajectory of a material point with fixed t_{inj}. Indeed, for a fixed t_{inj} (and hence fixed material point), plotting ζ_+ vs $1/(1-\psi)$ (with $1/(1-\psi) = t/t_{\text{inj}}$ via equation (3.2)) is just a rescaling of y vs t. The fact that this is not a straight line in Figure 3(b) indicates that, in the upper region, material point motion always varies with time even in the limit of very small t_{inj} and hence very small t: this is one of the challenges of tracking material points in the upper region.

5. Second order correction to front shape

To date all we have done is review the first order findings of [27], recast in terms of a more convenient variable set. Now we extend those findings to obtain a second order accurate solution in time to compute the upper and lower region of the front. Key results we obtain are equations (5.5)–(5.7), from which we can track upper region material points on the front, and equation (5.8), for which we can compute the corresponding location of points in the lower region. Some details are relegated to supplementary material.

(a) Second order location of the upper region's material points

Although we parameterise the system in terms of ψ here, if we recall that ζ and Ξ could also be expressed readily in terms of A (see equations (S 1.2) and (S 1.3), respectively), it is useful to begin by computing a second order expression for the front orientation angle A, for a small but finite time t (see supplementary material, section (a) for details of how this is achieved). It is reasonable to expand A as

$$A(\psi, t) \approx A_0(\psi) + t\, A_1(\psi), \tag{5.1}$$

in order to determine the effect of an order t correction upon the rescaled front orientation angle A (which corresponds to an order $t^{3/2}$ correction for α, see equation (3.1)). Equation (5.1) breaks the similarity solution, depending as it does on both ψ and t, not merely on ψ. Consistently, we can expand the rescaled vertical the rescaled vertical (see supplementary material, section (b) for details), and horizontal (see supplementary material, section (c) for details) location of the upper region's material points respectively, in the form of

$$\zeta(\psi, t) \approx \zeta_0(\psi) + t\, \zeta_1(\psi), \tag{5.2}$$

$$\Xi(\psi, t) \approx \Xi_0(\psi) + t\, \Xi_1(\psi). \tag{5.3}$$

Here, A_0, ζ_0 and Ξ_0 from section 3, and A_1, ζ_1 and Ξ_1 computed in supplementary material section S 5, turn out to be well defined quantities in terms of ψ. In addition, since ζ is related to y via equation (2.4) and Ξ is related to ξ via equation (2.7), and hence to x via equation (2.5), it follows that equations (5.2) and (5.3) are order t^2 and $t^{5/2}$ accurate expressions, in y and x respectively. To use these expressions to find the matching point between both regions of the front, we must also calculate, with a consistent order of accuracy, the shape of the lower region.

(b) Second order correction to lower region front shape

We now present an extension of the equation (2.9), used to compute the lower region of the front. Note that the equation (2.9), has been derived via an order $t^{3/2}$ accurate solution in the x direction (given by equation (2.1); also known as the improved Velde solution), and an order t accurate solution in the y direction (given by equation (2.2)). We need however, to incorporate the order t^2 effect, in the vertical, which is given by equation (2.11), along with an order $t^{5/2}$

correction to compute the x location of material points, to achieve the same order of accuracy as is computed for the upper region via equation (5.2) and (5.3). The required expression is (see supplementary material section S 3)

$$\Xi \approx \frac{1}{2\sqrt{2}}\left(\zeta - \frac{1}{6} + \frac{t}{8}\left(\zeta^2 - \frac{\zeta}{3} + \frac{107}{540}\right)\right), \quad \text{if} \quad \zeta \geq \zeta_{\text{cross}}, \tag{5.4}$$

which represents a parabola, as it includes a second order term in ζ. This is applicable specifically near the top of the lower region ($\zeta \geq \zeta_{\text{cross}}$ but not $\zeta \gg 1$). Here, we see how a self-similar solution (given by equation (2.9) involving only Ξ and ζ), valid for early times, is broken at a small but finite time. According to equation (5.4), for any specified ζ, the order t correction term for Ξ is positive, so on a graph such as Figure 3(a), which plots coordinates $(-\zeta,-\Xi)$, we obtain a point to the left of the $t \to 0$ limit (dotted line in Figure 3(a)).

(c) Rescaled location of the upper region's material points

The form of equations (5.1), (5.2), (5.3) (upper region), and (5.4) (lower region), indicates that in the limit $t \to 0$, the upper region can be expressed in similarity form via variables ζ and Ξ, in which for the upper region in particular, only the ratio $t_{\text{inj}}/t \equiv 1-\psi$ was relevant. Nevertheless, for small but finite t, the similarity solution is broken as alluded to earlier, and both values t_{inj} and t are needed. To explore how the similarity solution becomes broken, we can either select a given t and find the front shape ζ vs Ξ at that time, or alternatively we can select a given t_{inj} and find how a material point injected at time t_{inj} moves and reorients. This latter approach is easier since the governing equations for pressure-driven growth are expressed in Lagrangian form. A rescaling of the variables is now convenient. We define ζ_+ and Ξ_+, as the rescaled $1-y$ and $\sqrt{2t}-x$ front location, rescaling respectively, by amounts depending solely on the now fixed t_{inj} (respectively by $t_{\text{inj}}/2$ and $t_{\text{inj}}^{3/2}$), and we track a material point trajectory parametrically, by varying ψ from 0 up to ψ_{cross} (the matching point between the lower and upper region). Consistently, we define A_+ as the rescaled front orientation angle α, rescaled by $\sqrt{t_{\text{inj}}/2}$. Using definitions analogous to equations (2.4), (2.7), and (3.1), but with t_{inj} in place of t, and relating A_+, ζ_+ and Ξ_+ back to A, ζ and Ξ, we compute via equations (5.1)–(5.3)

$$A_+ \approx \frac{A_0(\psi)}{\sqrt{1-\psi}} + t\,\frac{A_1(\psi)}{\sqrt{1-\psi}} \equiv A_{+,0}(\psi) + t_{\text{inj}}\frac{A_1(\psi)}{(1-\psi)^{3/2}} = A_{+,0}(\psi) + t_{\text{inj}}\,A_{+,1}(\psi), \tag{5.5}$$

$$\zeta_+ \approx \frac{\zeta_0(\psi)}{1-\psi} + t\,\frac{\zeta_1(\psi)}{1-\psi} \equiv \zeta_{+,0}(\psi) + t_{\text{inj}}\,\frac{\zeta_1(\psi)}{(1-\psi)^2} = \zeta_{+,0}(\psi) + t_{\text{inj}}\,\zeta_{+,1}(\psi), \tag{5.6}$$

$$\Xi_+ \approx \frac{\Xi_0(\psi)}{(1-\psi)^{3/2}} + t\,\frac{\Xi_1(\psi)}{(1-\psi)^{3/2}} \equiv \Xi_{+,0}(\psi) + t_{\text{inj}}\frac{\Xi_1(\psi)}{(1-\psi)^{5/2}} = \Xi_{+,0}(\psi) + t_{\text{inj}}\,\Xi_{+,1}(\psi), \tag{5.7}$$

where t has been replaced by $t_{\text{inj}}/(1-\psi)$ (as follows from equation (3.2)). Hence, if we can determine how the front shape is perturbed at any given $t \ll 1$ (given by equations (5.1)–(5.3)), we can also determine how the trajectory of a material point is perturbed at any given t_{inj}, i.e, for different choices of $t_{\text{inj}} \ll 1$, we have different solutions of Ξ_+ and ζ_+ versus ψ, which correspond to the actual geometric path that a fixed injected material point takes (at least to second order accuracy) to reach the concave corner (the intersection with the lower region).

(d) Rescaled location of the lower region's material points

To find where material points injected in the upper region from time t_{inj} intersect the lower region, we convert (5.4) (applicable near the top of the lower region) into $\Xi_+ \equiv \Xi/(1-\psi)^{3/2}$ vs $\zeta_+ \equiv \zeta/(1-\psi)$ format. At any given time $t = t_{\text{inj}}/(1-\psi)$, it follows via equation (5.4)

$$\Xi_+ \approx \frac{(1-\psi)^{-3/2}}{2\sqrt{2}}\left(\zeta_+(1-\psi) - \frac{1}{6} + \frac{t_{\text{inj}}}{8}\left(\zeta_+^2(1-\psi) - \frac{\zeta_+}{3} + \frac{107}{540(1-\psi)}\right)\right) \tag{5.8}$$

where, given any $t_{\rm inj}$, our challenge is to find a ψ value (and hence a time t) at which equations (5.6) and (5.7) intersect equation (5.8). Therefore, equations (5.6) and (5.7) give a locus ζ_+ and Ξ_+ swept out by a material point in the upper region, and equation (5.8) gives the Ξ_+ that would be on the lower region at that same ζ_+. The upper and lower region only meet when, at the same ζ_+, they also have the same Ξ_+. This then gives the matching or cross-over $\zeta_{+\rm cross}$ and $\Xi_{+\rm cross}$ point: for additional details see section S 6 in supplementary material. Despite the similarity between equations (5.4) and (5.8), note the subtle difference in the way we use them. With equation (5.4) it is convenient to fix t, and consider how Ξ varies with ζ at that fixed t. With equation (5.8), however, we vary t (by varying ψ at given $t_{\rm inj}$), and select a particular ζ_+ (depending on ψ and hence on t), considering how Ξ_+ then varies. Therefore, tracking different $t_{\rm inj}$ gives different cross-over points $\zeta_{+\rm cross}$ and $\Xi_{+\rm cross}$, which can be expressed in a form giving the $\zeta_{\rm cross}$ and $\Xi_{\rm cross}$ location of the concave corner over time t: see section 6 and also supplementary material section S 7 for details. After using equation (5.8) in the way described above to locate the matching point, there turns out to be an alternative way in which this equation can be used. Given the ψ and ζ_+ values at the matching point, respectively $\psi_{\rm cross}$ and $\zeta_{+\rm cross}$, it is possible to find, for any given $t_{\rm inj}$, corresponding values of t and y at the matching point. For these specific t and y values, equation (2.11) can then be used to identify a y_0 value (i.e. a material point in the lower region, labelled by its initial location on the front) which coincides at the concave corner with the given upper region material point labelled by $t_{\rm inj}$. It turns out (see section S 8 in supplementary material) that the required y_0 only differs from unity by order $t_{\rm inj}$ amounts, so it is more useful to define a quantity $\mathfrak{z}_0 = 1 - y_0$ and hence a quantity Z_0

$$Z_0 \equiv (1 - y_0)/(t_{\rm inj}/2) = \mathfrak{z}_0/(t_{\rm inj}/2). \tag{5.9}$$

Once y_0 or equivalently Z_0 is known for any given $t_{\rm inj}$, then at all times t up the matching point, equation (2.11) can now be rescaled into ζ_+ vs ψ coordinates (see section S 8 in supplementary material for details), giving the trajectory followed by the lower region material point, generally having (at any given time t or equivalently at any given ψ) a ζ_+ different from the upper region material point (except at the matching point). Substituting the lower region ζ_+ into equation (5.8) and varying ψ gives the trajectory followed over time by this material point in terms of ζ_+ vs Ξ_+, which can be compared with the trajectory for the upper region material point described by equations (5.6)–(5.7). Trajectories of both points can be followed over time, and at the matching point, they coincide. Before equation (5.8) can be used in this particular fashion however, first the matching point itself must be found.

6. Perturbed location of the concave corner

In this section we present the perturbation analysis to track the location of the concave corner with second order accuracy in time. The key result is equation (6.7), giving the vertical location of the concave corner over time. This is what we contrast, in section 7, with the first order solution for the corner given by equation (4.1). The analysis proceeds as follows. Given a set of small but finite $t_{\rm inj}$ values here, we can obtain different $\psi_{\rm cross}$ values, with which we can determine the variation in location of the concave corner over time. In the limit when $t_{\rm inj} \to 0$, the value we seek is the aforementioned $\psi_{\rm cross} \approx 0.9431$ (which we now denote $\psi_{{\rm cross},0}$). More generally however, varying $t_{\rm inj}$, will cause $\psi_{\rm cross}$ (obtained as per the procedure discussed in section 5(d)) to vary also. In the limit of sufficiently small $t_{\rm inj}$, we can approximate this variation via

$$\psi_{\rm cross} \approx \psi_{{\rm cross},0} + t_{\rm inj}\psi_{{\rm cross},1} \approx \psi_{{\rm cross},0} + (1 - \psi_{{\rm cross},0})\psi_{{\rm cross},1}\, t. \tag{6.1}$$

Here, as mentioned above, $\psi_{{\rm cross},0}$ is the lowest order approximation found previously, and $\psi_{{\rm cross},1}$ is a next order correction to be determined. Knowing $\psi_{\rm cross}$, we can also define additional quantities $t_{\rm max}$ and $t_{{\rm inj}({\rm min})}$ (mentioned in section 4 and defined in supplementary material section S 2). Substituting (6.1) into equation (S 2.2) and Taylor expanding, we deduce that the

maximum time $t = t_{\max}$ for which a material point injected at $t_{\rm inj}$ could survive would be

$$t_{\max} \equiv \frac{t_{\rm inj}}{(1-\psi_{\rm cross})} \approx \frac{t_{\rm inj}}{1-\psi_{\rm cross,0}} + \frac{t_{\rm inj}^2 \psi_{\rm cross,1}}{(1-\psi_{\rm cross,0})^2}, \tag{6.2}$$

Moreover, at the cross-over point, the earliest injected material point still surviving at time t has $t_{\rm inj} = t_{\rm inj(min)}$ with, according to equations (6.1) and (S 2.1)

$$t_{\rm inj(min)} \equiv (1-\psi_{\rm cross})t \approx (1-\psi_{\rm cross,0})\, t - (1-\psi_{\rm cross,0})\psi_{\rm cross,1}\, t^2. \tag{6.3}$$

Although the discussion of sections 5(c)–(d) focussed on functions used for tracking loci of material points, i.e. fixed $t_{\rm inj}$, having the value of $t_{\rm inj(min)}$ can also be useful. Knowing $t_{\rm inj(min)}$ makes it possible to reconstruct the shape of the upper region (fixed t), by selecting a set of injected points $t_{\rm inj}$ in the domain $t_{\rm inj(min)} \le t_{\rm inj} \le t$. Then, computing $\psi = 1 - t_{\rm inj}/t$ for each one, and computing Ξ and ζ (given by equations (5.3) and (5.2), respectively) for each ψ at the given time t, we can reconstruct the front shape. Thus, we can convert between material point trajectories and front shapes. This will be explored further in section 8.

Once we know the values of $\psi_{\rm cross,0}$ and $\psi_{\rm cross,1}$, we can determine the perturbed value of A_+ at the concave corner (denoted $A_{+\rm cross}$) by using equation (5.5), as

$$A_{+\rm cross} \approx A_{+,0}(\psi_{\rm cross,0} + t_{\rm inj}\psi_{\rm cross,1}) + t_{\rm inj}\, A_{+,1}(\psi_{\rm cross,0} + t_{\rm inj}\psi_{\rm cross,1}), \tag{6.4}$$

which upon expanding for sufficiently small $t_{\rm inj}$ gives

$$\begin{aligned} A_{+\rm cross} &\approx A_{+,0}(\psi_{\rm cross,0}) + t_{\rm inj}\left(\psi_{\rm cross,1} A'_{+,0}(\psi_{\rm cross,0}) + A_{+,1}(\psi_{\rm cross,0})\right) \\ &\equiv A_{+\rm cross,0} + t_{\rm inj} A_{+\rm cross,1}, \end{aligned} \tag{6.5}$$

where $A'_{+,0}$ denotes the function $\mathrm{d}A_{+,0}/\mathrm{d}\psi$ (which is obtained via equations (3.3) and (5.5)). There are analogous expressions for ζ_+ and Ξ_+ at the concave corner (denoted $\zeta_{+\rm cross}$ and $\Xi_{+\rm cross}$): the formulae are given in equations (S 7.1)–(S 7.3) in supplementary material section S 7. There are also analogous expressions, but expanded in terms of t rather than in terms of $t_{\rm inj}$. These provide the cross-over values of A, ζ and Ξ, denoted $A_{\rm cross}$, $\zeta_{\rm cross}$ and $\Xi_{\rm cross}$: see equations (S 7.5)–(S 7.7) in supplementary material.

Various ways to estimate the location of the concave corner, in an effort to improve upon the first order estimate $y_{\rm 1st,cross}$ already given in equation (4.1), now present themselves. Based on the definition of $\zeta_+ \equiv (1-y)/(t_{\rm inj}/2)$, we can obtain, by tracking the vertical location of a given injected material point $t_{\rm inj}$ over time up to its intersection with the concave corner, an estimate of the y location of the corner. We denote this by $y^{\rm inter}_{\rm cross}$, i.e. the value of the matching point determined by this intersection, and it turns out to be

$$y^{\rm inter}_{\rm cross} = 1 - (t_{\rm inj}/2)\, \zeta_{+\rm cross}(t_{\rm inj}). \tag{6.6}$$

Here $\zeta_{+\rm cross}(t_{\rm inj})$ is obtained as already mentioned by tracking $t_{\rm inj}$ on the upper region using equations (5.6)–(5.7), until its location coincides with the lower region given by equation (5.8). The value of $\zeta_{+\rm cross}(t_{\rm inj})$ determined here will not agree perfectly with the expression obtained via a small $t_{\rm inj}$ expansion for $\zeta_{+\rm cross}$ (see equation (S 7.2) in supplementary material), although agreement should be good when $t_{\rm inj}$ is sufficiently small. We can combine this expression for $y^{\rm inter}_{\rm cross}$ vs $t_{\rm inj}$ with an expression for time at cross-over $t = t_{\rm inj}/(1-\psi_{\rm cross})$ vs $t_{\rm inj}$, this latter expression again not agreeing perfectly with the Taylor expanded form given in (6.2). Despite these small discrepancies, a parametric representation of the cross-over y vs time t can now be obtained by varying $t_{\rm inj}$. A slightly different estimate for the second order vertical location of the concave corner over time t, can be obtained by combining equation (2.10) with a small t expansion for $\zeta_{\rm cross}$ in equation (S 7.6), obtaining

$$y_{\rm 2nd,cross} \approx 1 - (t/2)\, \zeta_{\rm cross,0} - (t^2/2)\, \zeta_{\rm cross,1}. \tag{6.7}$$

In the limit of sufficiently small t, this should agree with what (6.6) predicts, but is rather simpler to evaluate. Provided we can determine $\zeta_{\rm cross,1}$ (the value of $\zeta_{\rm cross,0}$ being already known from

literature [27]; see also Table 1 later on), we can estimate the second order position of the concave corner over time. Predictions for how second order effects perturb not only the concave corner but also material point trajectories are discussed in the next section.

7. Second order matching between upper and lower region

In this section, we determine the effect of selecting a small but finite time upon the evolution of the upper region of the front, and how the matching point between the lower and the upper region moves with time. Recall that we are working with second order accuracy in time, in the sense that we have included an order t^2 correction (newly derived here for the upper region, but already given by [27] in the case of the lower region) to compute vertical location y, and an order $t^{5/2}$ expression in time (newly derived in the present work) to compute the horizontal position x or ξ of a material point, with a consistent order of accuracy in time for both, upper and lower region. After suitable rescaling, this is given by equations (5.2) and (5.3) for the upper region, and equation (5.4) for the lower region. In order to measure the concave corner location over time, we use equations (5.7) and (5.6) to compute the (Ξ_+, ζ_+) location of the upper region's material points, which is done by fixing t_{inj} (following the trajectory of a specific material point), and then tracking (parametrically in terms of ψ) the locus swept out by the material point, up to the matching point with the lower region, with a (Ξ_+, ζ_+) location given by equation (5.8). To find the intersection where the two regions meet (see the discussion in section 5(d)), it is sufficient to focus on a point in the lower region with the same ζ_+ value as the material point in the upper region, and determine the corresponding Ξ_+ value via (5.8). This is what is plotted in Figure 2 in section S 6 in supplementary material. When the location of the matching point is found however, we can identify which specific material point from the lower region (identified by the value of Z_0 via equation (5.9)) happens to be present there (again see the discussion in section 5(d) and details in section S 8). Then trajectories of both upper and lower region material points can be tracked until their intersection. This is what is plotted here in Figure 4.

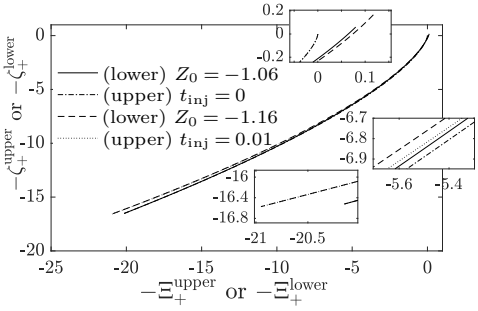

Figure 4: Trajectory of fixed material points labelled by t_{inj} in the upper region, and fixed material points labelled by $Z_0 \equiv (1 - y_0)/(t_{\text{inj}}/2)$ in the lower region in terms of rescaled vertical and horizontal distances ζ_+ and Ξ_+. Dash-dotted line for upper region $t_{\text{inj}} = 0$ vs solid line for lower region $Z_0 \approx -1.06$ (see section S 8 in supplementary material for explanation of how to determine this Z_0 value). Dotted line for $t_{\text{inj}} = 0.01$ vs dashed line for $Z_0 \approx -1.16$. The curves are close to overlapping along almost all the trajectory, although they only intersect at the matching point $(\Xi_{+\text{cross}}, \zeta_{+\text{cross}})$.

In Figure 4, we see that the matching point is slightly sensitive to t_{inj}. Increasing t_{inj} causes it to shift the left (i.e. larger Ξ_+) and also slightly downwards (larger ζ_+). We also note Figure 4 that values of Z_0 are negative (see more explanation in the supplementary material section S 8). This implies y_0 values in excess of unity, i.e. points not actually present on the front initially, but which instead are extracted from the corner into the lower region as the system evolves.

Although Figure 4 only shows two $t_{\rm inj}$ values ($t_{\rm inj}\to 0$ and $t_{\rm inj}=0.01$) we have repeated the calculations for a number of $t_{\rm inj}$ values in the domain $t_{\rm inj}\in[0,0.01]$, determining in each case the ψ value, namely $\psi_{\rm cross}$, at which these points meet the concave corner (see Figure 5) and hence the maximum survival time $t_{\max}(t_{\rm inj})$, which is also estimated at least for $t_{\rm inj}\ll 1$ by equation (6.2) (see Figure 6). We can also compute A_+, ζ_+, and Ξ_+ at the concave corner (see Figures 7(a)–(c)), and then (by employing equations (5.5)–(5.7)), A, ζ, and Ξ values there (see Figures 7(d)–(f)). These expressions plotted in Figure 7 break similarity by allowing separate dependence on $t_{\rm inj}$ and t, rather than holding all values fixed at the matching point. At sufficiently small $t_{\rm inj}$ and/or t we expect variation in all the above mentioned quantities to be linear in $t_{\rm inj}$ and/or t, as established by equations (S 7.1)–(S 7.3) and (S 7.5)–(S 7.7), respectively (as given in supplementary material section S 7). Here, we achieve this by focussing firstly on exceedingly small times $t_{\rm inj}\in[0,0.0001]$, thereby obtaining parameters for equations (6.1), (S 7.1)–(S 7.3), (S 7.5)–(S 7.7) and subsequently for (6.7), i.e. we obtain firstly $\psi_{\rm cross,0}$ and $\psi_{\rm cross,1}$ using data for $t_{\rm inj}\in[0,0.0001]$, from which we compute $A_{+{\rm cross},0}$, $A_{+{\rm cross},1}$, $\zeta_{+{\rm cross},0}$, $\zeta_{+{\rm cross},1}$, $\Xi_{+{\rm cross},0}$ and $\Xi_{+{\rm cross},1}$, and subsequently $A_{{\rm cross},0}$, $A_{{\rm cross},1}$, $\zeta_{{\rm cross},0}$, $\zeta_{{\rm cross},1}$, $\Xi_{{\rm cross},0}$ and $\Xi_{{\rm cross},1}$. These values are summarized in Table 1. Note that although $A_{{\rm cross},0}$, $\zeta_{{\rm cross},0}$ and $\Xi_{{\rm cross},0}$, can be straightforwardly expressed in terms of $A_{+{\rm cross},0}$, $\zeta_{+{\rm cross},0}$ and $\Xi_{+{\rm cross},0}$ and $\psi_{{\rm cross},0}$ (see equations (5.5)–(5.7)), the relations for $A_{{\rm cross},1}$, $\zeta_{{\rm cross},1}$ and $\Xi_{{\rm cross},1}$ in equations (S 7.5)–(S 7.7), are rather more complex, and these quantities can even have opposite sign from $A_{+{\rm cross},1}$, $\zeta_{+{\rm cross},1}$ and $\Xi_{+{\rm cross},1}$ in equations (S 7.1)–(S 7.3), as in fact is obtained here (see Table 1). How such sign changes can arise is discussed in section S 7.

$\psi_{\rm cross,0}$	$\psi_{\rm cross,1}$	$A_{+{\rm cross},0}$	$A_{+{\rm cross},1}$	$\zeta_{+{\rm cross},0}$	$\zeta_{+{\rm cross},1}$	$\Xi_{+{\rm cross},0}$	$\Xi_{+{\rm cross},1}$
0.9431	0.4608	4.94	16.11	16.52	81.64	20.15	211.28
		$A_{{\rm cross},0}$	$A_{{\rm cross},1}$	$\zeta_{{\rm cross},0}$	$\zeta_{{\rm cross},1}$	$\Xi_{{\rm cross},0}$	$\Xi_{{\rm cross},1}$
		1.1784	−0.0528	0.9397	−0.1686	0.2733	−0.0257

Table 1: Parameters for equations (6.1), (S 7.1)–(S 7.3), (S 7.5)–(S 7.7) (given in section S 7 in supplementary material), and (6.7).

The above mentioned sign changes have the following implication. In a view such as Figure 4, $-\Xi_+$ vs $-\zeta_+$, which compares trajectories of material points released at different $t_{\rm inj}$, we have already seen that increasing $t_{\rm inj}$ drives the concave corner to the left and downwards, with the leftward shift being particularly noticeable due to the large $\Xi_{+{\rm cross},1}$ value in Table 1. On the other hand, since $\zeta_{{\rm cross},1}$ and $\Xi_{{\rm cross},1}$ are negative, snapshots of the instantaneous front shape at various times t, using now $-\zeta$ vs $-\Xi$ coordinates in a view similar to Figure 3(a), would show the corner shifting upwards and to the right, the upward shift being dominant owing to $\Xi_{{\rm cross},1}$ in Table 1 being very small. In addition, the negative value of $A_{{\rm cross},1}$ implies that the jump in angle at the concave corner is less than first order theory predicts, but since $A_{{\rm cross},1}$, like $\Xi_{{\rm cross},1}$, is numerically small in Table 1, the shift in jump angle is likewise small, compared with the vertical shift of the corner. The fact that fixing t produces a vertical shift in the corner location, whereas fixing $t_{\rm inj}$ produces a horizontal shift, indicates how the similarity solution breaks down, i.e. the solution no longer depends solely on the ratio $t_{\rm inj}/t$.

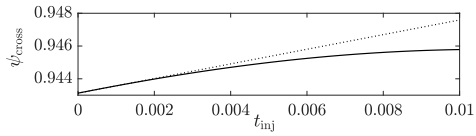

Figure 5: ψ_{cross} as a function of t_{inj}. Solid line: Value ψ_{cross} of the matching point tracked up to time $t_{\text{inj}} = 0.01$. Dotted line: linear approximation obtained from data up to time $t_{\text{inj}} = 0.0001$, with $\psi_{\text{cross}} \approx \psi_{\text{cross},0} + t_{\text{inj}}\psi_{\text{cross},1}$ and for $\psi_{\text{cross},0} \approx 0.9431$ and $\psi_{\text{cross},1} \approx 0.4608$.

We now return to consider t_{inj} values in the domain, $t_{\text{inj}} \in [0, 0.01]$, instead of the much narrower domain $t_{\text{inj}} \in [0, 0.0001]$ used to obtain the data of Table 1. In Figure 5 we see ψ_{cross} as a function of t_{inj}, and it is clear that only for small times ($t_{\text{inj}} \leq 0.002$) we can consider the relation for ψ_{cross} to be a linear function well approximated by $\psi_{\text{cross}} \approx \psi_{\text{cross},0} + t_{\text{inj}}\psi_{\text{cross},1}$ (given by equation (6.1)), with values of $\psi_{\text{cross},0}$ and $\psi_{\text{cross},1}$ given by Table 1. Nonetheless, at least on the domain of Figure 5, we found that as t_{inj} increases, the matching point ψ_{cross} still manages to increase albeit deviating from equation (6.1). The values of ψ_{cross} now affect the behaviour of a number of other quantities ($t_{\max}$, $t_{\text{inj(min)}}$ as well as $A_{+\text{cross}}$, $\zeta_{+\text{cross}}$, $\Xi_{+\text{cross}}$, A_{cross}, ζ_{cross}, and Ξ_{cross}) as we explain below, with an impact in turn on the corner's vertical y coordinate location (as we go on to explain).

(a) Values of $t_{\max}$ vs t_{inj} and $t_{\text{inj(min)}}$ vs t

As has been indicated already in sections 4 and 6, for a given fixed t_{inj} we can calculate the maximum survival times $t_{\max}(t_{\text{inj}})$ (time at which the injected point t_{inj} reaches the concave corner). This is obtained by equations (S 2.2) (as given in the supplementary material) and/or via an expansion (6.2), and is what Figure 6(a) shows. Equivalently (see Figure 6(b)) for a given t we can determine the injection time $t_{\text{inj(min)}}$ of the earliest injected point still surviving (see equation (6.3)). From the data in Figure 5 and Table 1, specifically via the linear approximation of ψ_{cross} in (6.1), we evaluate equations (6.2) and (6.3), as

$$t_{\max}/t_{\text{inj}} \approx 17.57 + 142.33\, t_{\text{inj}}, \tag{7.1}$$

$$t_{\text{inj(min)}}/t \approx 0.0569 - 0.0262\, t, \tag{7.2}$$

which are also plotted in Figures 6(a) and (b), respectively. Overall, equations (7.1) and (7.2) represent, at least for small time, good approximations to $t_{\max}$ and $t_{\text{inj(min)}}$. Note in particular that $t_{\text{inj(min)}}/t \equiv 1 - \psi_{\text{cross}}$ (see equation (S 2.1) in the supplementary material) so the data in Figure 6(b) mirror those in Figure 5.

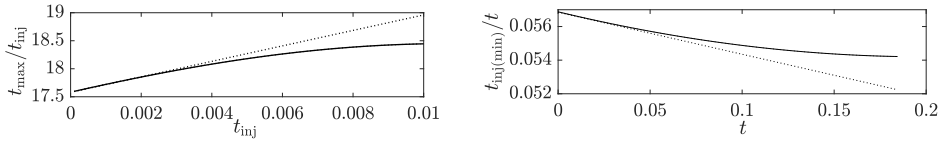

(a) (b)

Figure 6: (a) Maximum survival time, for a given injected material point. Solid line: $t_{\max}/t_{\text{inj}}$ vs t_{inj}, given by equation (S 2.2) (as given in the supplementary material). Dotted line: approximation given by equation (7.1). (b) Minimum injection time of all surviving material points as a function of time. Solid line: $t_{\text{inj(min)}}/t$ vs t, given by equation (S 2.1). Dotted line: approximation given by equation (7.2).

(b) Values of $A_{+\mathrm{cross}}$, $\zeta_{+\mathrm{cross}}$, $\Xi_{+\mathrm{cross}}$, A_{cross}, ζ_{cross}, and Ξ_{cross}

Using ψ_{cross} obtained from Figure 5 we can also determine evolution of the orientation and position of the concave corner over time, by evaluating either equations (5.5)–(5.7) or equations (5.1)–(5.3) setting also $t = t_{\max}(t_{\mathrm{inj}})$ via Figure 6(a). The behaviour we observe is as follows (see Figure 7). In Figures 7(a)–(c) we see how $A_{+\mathrm{cross}}$, $\zeta_{+\mathrm{cross}}$ and $\Xi_{+\mathrm{cross}}$ (i.e. values at the concave corner), respectively, increase at early times as t_{inj} increases, and then, at slightly larger t_{inj}, they are predicted to decrease. In contrast, in Figures 7(d)–(f), we see how A_{cross}, ζ_{cross} and Ξ_{cross}, respectively, decrease as time t increases. The implications of these findings for ζ_{cross} in particular are discussed next.

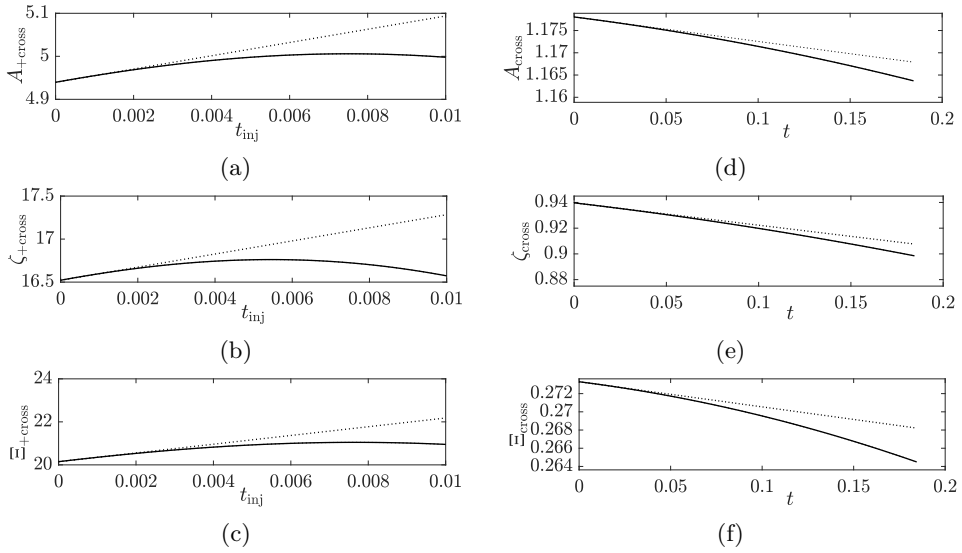

Figure 7: Values of variables at the matching point over time t_{inj} or t. Different computations of (a) $A_{+\mathrm{cross}}$, (b) $\zeta_{+\mathrm{cross}}$, and (c) $\Xi_{+\mathrm{cross}}$ for $t_{\mathrm{inj}} \leq 0.01$. These are obtained respectively by equations (5.5)–(5.7) evaluated at ψ_{cross} (solid lines), and by equations (S 7.1)–(S 7.3) (dotted lines), with parameters as shown in Table 1. (d) A_{cross}, (e) ζ_{cross} and (f) Ξ_{cross}, for $t = t_{\max}(t_{\mathrm{inj}}) = t_{\mathrm{inj}}/(1-\psi_{\mathrm{cross}})$, with $t_{\mathrm{inj}} \leq 0.01$, which are obtained respectively by equations (5.1)–(5.3) evaluated at ψ_{cross} (solid lines), and by equations (S 7.5)–(S 7.7) (dotted lines), with parameters as shown in Table 1.

(c) Data for corner's vertical location

As can be seen in Figure 7(e), ζ_{cross} decreases with increasing t, which has an important implication: the vertical location of the concave corner is higher up in y than was predicted at leading order. Using equation (6.7) for the vertical location of the concave corner over time, along with data from Table 1 fed into equation (S 7.6) we can deduce

$$y_{\mathrm{2nd,cross}} \approx 1 - 0.4698t + 0.0843\,t^2. \tag{7.3}$$

This is plotted in Figure 8, representing an improvement over and above the formula $y_{\mathrm{1st,cross}}$ given by equation (4.1) (also plotted in Figure 8). In this same figure we also show (obtained parametrically by varying t_{inj}) values computed for $y^{\mathrm{inter}}_{\mathrm{cross}} = 1 - (t_{\mathrm{inj}}/2)\zeta_{+\mathrm{cross}}$, as given by equation (6.6), vs $t = t_{\max} \equiv t_{\mathrm{inj}}/(1-\psi_{\mathrm{cross}}(t_{\mathrm{inj}}))$ as given by equation (S 2.2) in the supplementary material. That this parametric expression for $y^{\mathrm{inter}}_{\mathrm{cross}}$ vs t must agree well with equation (7.3) for sufficiently small t follows from the two curves as seen in Figure 7(e) initially having the same slope. As t increases though (albeit well beyond the domain plotted

in Figure 7(e)) considerable deviation sets in between $y^{\text{inter}}_{\text{cross}}$ and $y_{2\text{nd,cross}}$, and this is what we see in Figure 8. This is mainly associated with the $\zeta_{+\text{cross}}$ values obtained within equation (6.6) falling well below the predictions of a small t_{inj} expansion given by equation (S 7.2), ultimately leading to $y^{\text{inter}}_{\text{cross}}$ values exceeding $y_{2\text{nd,cross}}$. Moreover, we plot an Eulerian predicted position of the concave corner, a numerical result given by [32]

$$y_{\text{Eulerian}} = 1 - 0.4635t + 0.0784t^2, \tag{7.4}$$

obtained via interpolation of numerical data, fitted over a domain $t \in [0, 2]$, in a space domain $x \in [0, 2]$, $y \in [0, 1]$, where the grid size for the solution variable in the numerical Eulerian method [32] was $\Delta x = \Delta y = 2.5 \times 10^{-3}$, with the time step Δt set via the Courant-Friedrichs-Lewy condition (CFL) [34]. Over the domain Figure 8 these Eulerian data are evidently close to $y_{2\text{nd,cross}}$ data but further away from the data for $y^{\text{inter}}_{\text{cross}}$. We have also plotted the trajectory of the topmost point of the lower region $y_{2\text{nd,lower}}$ given by equation (2.12), via a second order approximation (see Figure 8).

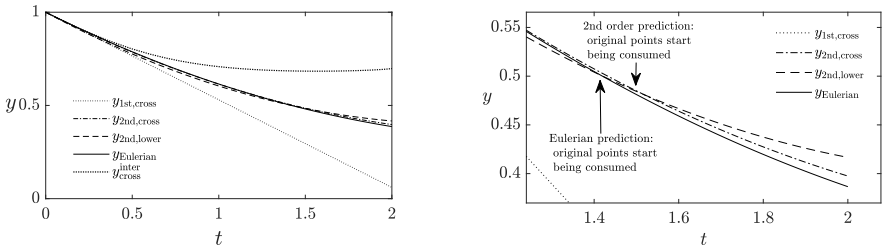

(a) (b)

Figure 8: Vertical y position of the concave corner as a function of time t. (a) Dotted line: first order solution $y_{1\text{st,cross}}$ given by equation (4.1). Dash-dotted line: Second order solution $y_{2\text{nd,cross}}$ given by equation (7.3). Dashed line: Solution for a material point originally at the top of the lower region $y_{2\text{nd,lower}}$, see equation (2.12). Solid line: Eulerian numerical solution y_{Eulerian}, obtained in time domain $t \in [0, 2]$ with a grid spacing of $\Delta x = \Delta y = 2.5 \times 10^{-3}$, and Δt adjusted via CFL condition [32]. Dense-dotted line: Solution $y^{\text{inter}}_{\text{cross}}$ given by equation (6.6). (b) Zoomed view of (a) at later times. We show via Eulerian vs via the current second order prediction, the estimated point where material points originally on the front at time $t = 0$ start being consumed (at which $y_{2\text{nd,lower}}$ moves above the concave corner).

By comparing $y_{2\text{nd,lower}}$ with the position of the concave corner obtained via our $y_{2\text{nd,cross}}$ we can determine that not only are material points from the upper region being consumed by the concave corner (which follows because $t_{\text{inj(min)}} = (1 - \psi_{\text{cross}})t$ is an increasing function of time), but also that material points must initially be extracted from the concave corner in order to populate the lower region, as early on $y_{2\text{nd,lower}}$ is below $y_{2\text{nd,cross}}$. This however only appears to happen until a certain time after which points of the lower region start being consumed by the concave corner. Indeed at a certain time $y_{2\text{nd,lower}}$ intersects the concave corner (see Figure 8(b)): all extracted points have now been consumed. So, initially new points are extracted into the lower region, then those same points are consumed, after which the points originally present in the lower region start being consumed.

We have currently several different methods to estimate the position of the concave corner, hence different estimates of when $y_{2\text{nd,lower}}$ and the concave corner might coincide. Via the first order analytical solution for the corner $y_{1\text{st,cross}}$, compared to $y_{2\text{nd,lower}}$, we could determine that originally present points start being consumed by the concave corner from time $t \approx 0.289$ at $y \approx 0.864$, although this result is likely to be unreliable employing as it does $y_{1\text{st,cross}}$. Meanwhile the point $y^{\text{inter}}_{\text{cross}}$ never coincides with $y_{2\text{nd,lower}}$ for any $t > 0$. However, the second order solution

for the corner $y_{2\mathrm{nd,cross}}$ coincides with $y_{2\mathrm{nd,lower}}$ at time $t \approx 1.518$ at $y \approx 0.481$. On the other hand, using the corner location as predicted via the Eulerian method, we determine that material points originally present in the lower region start being consumed by the concave corner at time $t \approx 1.416$ at $y \approx 0.501$ (see Figure 8(b)). At the comparatively large times considered here, there is difference among the various predictions. The difference is unsurprising, since our first and second order analytical solution are formally small time expansions, so we do not expect them to be valid all the way up to $t = 2$. To quantify deviations between the Eulerian data and the various other solutions that we have derived, we measure the root-mean-square (rms) error with respect to the Eulerian data, up to $t = 2$. The rms error between y_{Eulerian} and $y_{1\mathrm{st,cross}}$ turned out to be 0.1473, between y_{Eulerian} and $y_{\mathrm{cross}}^{\mathrm{inter}}$ it was 0.1518, and between y_{Eulerian} and $y_{2\mathrm{nd,cross}}$ it was 0.0039. This proves that the second order solution given by equation (7.3) gives a much better estimate for the concave corner position over time than the first order solution does, as expected. In addition, the rms difference between y_{Eulerian} and $y_{2\mathrm{nd,lower}}$ was found to be 0.0118, which is larger than the error between y_{Eulerian} and $y_{2\mathrm{nd,cross}}$. The difference between y_{Eulerian} and $y_{2\mathrm{nd,cross}}$ must come from either higher order corrections in time (and hence not captured equations (5.1)–(5.3) nor by $y_{2\mathrm{nd,cross}}$) or else truncation error in the numerical scheme used to obtain y_{Eulerian}. Since the difference between y_{Eulerian} and $y_{2\mathrm{nd,lower}}$ is however larger than this, we assert that the difference between $y_{2\mathrm{nd,lower}}$ and the location of the concave corner is genuine and not solely due to error in our second order expansion. Thus, we confirm that we are actually extracting material points to populate the lower region at early times, but later on, we consume those extracted points again. However, doubt is still present, regarding the exact time at which material points originally present on the front start being consumed, as our estimates require extrapolation out of the $t \ll 1$ domain where second order solutions formally apply.

In summary, we found that our second order predicted location of the concave corner fits the Eulerian data reasonably well, at both, small times $t \ll 1$ and also up to times of order unity. Nevertheless, for points away from the concave corner, we have not yet demonstrated whether the position of the Lagrangian material points forming the upper region fit front shape predictions from the Eulerian numerical data. This will be considered in the next section.

8. Second order front shape at later times

In order to check reliability of our second order results, we compute for a given time $t = 1$, the front shape $(-\Xi, -\zeta)$ (see Figure 9(a)), as a collection of material points with different t_{inj} all at the same t, specifically $t = 1$. Thus, we fix t and vary t_{inj} from $t_{\mathrm{inj(min)}}$ to t, by varying ψ, from 0 up to ψ_{cross}. We plot $(-\Xi, -\zeta)$ at both first order (equations (3.4)–(3.5)) and second order (equations (5.2)–(5.3)) comparing results with the numerical Eulerian data. When $t = 1$, the first order theory predicts $t_{\mathrm{inj(min)}} = 1 - \psi_{\mathrm{cross},0} \approx 0.0569$ whereas the second order procedure (i.e. tracking (5.6)–(5.7) until they match with (5.8)) requires $t_{\mathrm{inj(min)}} \approx 0.0997$ to achieve matching at $t = 1$. This is already outside the domain $t_{\mathrm{inj}} \in [0, 0.01]$ analysed in section 7, and likewise outside the domain in which we can apply equation (7.2) to estimate t_{inj} given t. A value $t_{\mathrm{inj(min)}} \approx 0.0997$ when $t = 1$ implies $\psi_{\mathrm{cross}} \approx 0.9003$ in order for equations (5.6)–(5.7) and (5.8) to match, which is actually less than the value of $\psi_{\mathrm{cross},0}$. It follows that ψ_{cross} initially increases as t_{inj} increases (as per Figure 5) but for large t_{inj} it starts to decrease. In addition to front shape data $(-\Xi,-\zeta)$ as plotted in Figure 9(a), we also show, in Figure 9(b), the orientation angle A versus ζ. For the upper region, this is given parametrically, in terms of $A_0(\psi)$ and $\zeta_0(\psi)$ (at first order), and $A(\psi, t)$ and $\zeta(\psi, t)$ (at second order), via equations (3.3), (3.4), (5.1) and (5.2). We also plot the lower region angle $A(t)$ vs $\zeta(t)$, which is determined either using equation (2.1) (accurate to order $t^{3/2}$ in x) or else via (S 3.6) (in supplementary material; accurate to order $t^{5/2}$ in x) coupled with equation (2.11). The upper and lower region predictions are compared with Eulerian data, although in Figure 9(b), these display oscillations in the neighbourhood of the concave corner, which are just numerical artifacts [32]. In Figure 9(a), we see how the self-similar nature of ζ and Ξ, present at early times, is broken at a finite time $t = 1$. Here, we also appreciate how the upper region given by equations (5.2) and (5.3), intersects the lower

region given by equation (5.4), at $\zeta(\psi_{\rm cross}, t=1) \approx 0.5839$ and $\Xi(\psi_{\rm cross}, t=1) \approx 0.1627$, with $\psi_{\rm cross} \approx 0.9003$ (horizontal line labelled by {1} in Figure 9(a)). This point corresponds to a y value of $y^{\rm inter}_{\rm cross}$ at $t=1$ (see Figure 8). Nevertheless, we extend the second order solution via a linear extrapolation up to the point where equation (S 7.6) would predict the location of the concave corner (see section S 9 in supplementary material for details), suggesting instead $\zeta_{\rm cross}(t=1) \approx 0.7711$ (horizontal line labelled by {2} in Figure 9(a)). This now corresponds to a y value of $y_{\rm 2nd,cross}$ at $t=1$ (see Figure 8). Here also we see that our current second order solution for ζ vs Ξ is closer to the Eulerian data, than the first order solution is. Indeed the dotted curve, corresponding to the upper region via a first order approximation $(\zeta_0(\psi), \Xi_0(\psi))$, finishes even further away, with $\zeta_{\rm cross,0} \approx 0.9397$ and $\Xi_{\rm cross,0} \approx 0.2733$ (values quoted in Table 1; see horizontal line labelled by {3} in Figure 9(a) corresponding to $y_{\rm 1st,cross}$ in Figure 8), intercepting the lower region predicted by (4.1) (thick-dotted line).

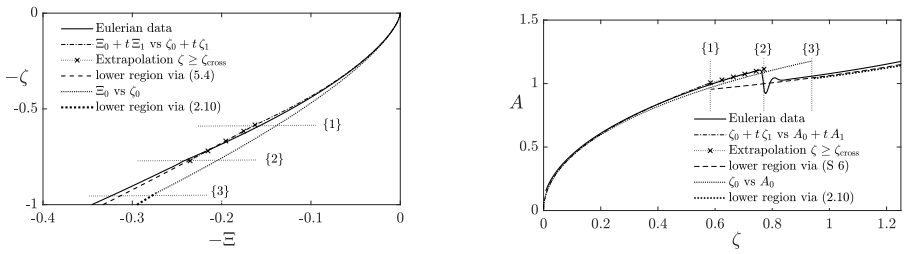

Figure 9: (a) Front shape $(-\Xi, -\zeta)$ at time $t=1$, via first and second order solution, for upper and lower region, compared with Eulerian data. Solid line: Eulerian data. Dash-dotted line: second order approximation $\zeta_0(\psi) + t\,\zeta_1(\psi)$ and $\Xi_0(\psi) + t\,\Xi_1(\psi)$ for the upper region, given by equations (5.2) and (5.3), respectively, up to intersection with the lower region (dashed line) computed via equation (5.4). At time $t=1$, the intersection occurs at $\zeta(\psi_{\rm cross}) \approx 0.5839$ with $\Xi(\psi_{\rm cross}) \approx 0.1627$, horizontal line labelled by {1}. We have however computed ζ vs Ξ further than this ("$\times$" line; see section S 9 in supplementary material for details), up to a ζ value obtained by extrapolating the prediction of equation (S 7.6) up to $t=1$, which gives $\zeta_{\rm cross}(t=1) \approx 0.7711$ (horizontal line labelled by {2}), with a corresponding value of $\Xi \approx 0.2353$ (this value is slightly different from that predicted by extrapolation of equation (S 7.7), which gives instead $\Xi_{\rm cross}(t=1) \approx 0.2476$). Dotted line: first order approximation $\zeta_0(\psi)$ and $\Xi_0(\psi)$ for the upper region, given by equations (3.4) and (3.5), up to the intersection with the lower region via equation (2.9) (thick-dotted line), with $\zeta_{\rm cross,0} \approx 0.9397$ and $\Xi_{\rm cross,0} \approx 0.2733$ (horizontal line labelled by {3}). (b) Rescaled front orientation angle A vs rescaled vertical coordinate ζ. Solid line: Eulerian data. Dash-dotted line: second order approximation $A_0(\psi) + t\,A_1(\psi)$ and $\zeta_0(\psi) + t\,\zeta_1(\psi)$ for the upper region, given by equations (5.1) and (5.2), computed at time $t=1$ up to the intersection with the lower region (given by equation (5.4)), which occurs at $A(\psi_{\rm cross}) \approx 1.0063$ with $\zeta(\psi_{\rm cross}) \approx 0.5839$ (vertical line labelled by {1}), with $\psi_{\rm cross} \approx 0.9003$. We have however computed A vs ζ further than this ("$\times$" line; see section S 9 in supplementary material for details), up to a value of ζ (vertical line labelled by {2}) obtained as before by extrapolating equation (S 7.6), $\zeta_{\rm cross}(t=1) \approx 0.7711$, and a corresponding value of $A \approx 1.1131$ (note that this value is slightly different from that predicted by extrapolation of equation (S 7.5), which gives $A_{\rm cross}(t=1) \approx 1.1259$). Here we can also see the lower region computed via equation (5.4) (dashed line) obtained for $\zeta \geq \zeta(\psi_{\rm cross}) \approx 0.5839$, i.e. starting from vertical line labelled by {1}. Dotted line: first order approximation $A_0(\psi)$ and $\zeta_0(\psi)$ for the upper region, given by equations (3.3) and (3.4), respectively. Thick-dotted line: lower region computed via equation (2.1), for $\zeta > \zeta_{\rm cross,0}$ (vertical line labelled by {3}). We see that {2} agrees better with the Eulerian prediction of the corner location than {1} does.

In addition, we see that the lower region (given by second order equation (5.4) at least for parts of the lower region near the concave corner), is relatively close to the Eulerian solution, more so than first order equation (2.9). In Figure 9(b), we show the orientation angle A vs ζ, highlighting, as in Figure 9(a), the second order matching procedure (vertical line labelled {1} in Figure 9(b), corresponding to $y_{\rm cross}^{\rm inter}$), data extended up to the concave corner location predicted by equation (S 7.6) (vertical line labelled {2} in Figure 9(b), corresponding to $y_{\rm 2nd,cross}$), and we also show the intersection between the two regions via the first order solution (vertical line labelled {3} in Figure 9(b), corresponding to $y_{\rm 1st,cross}$). The value of $A(\psi_{\rm cross}) \approx 1.0063$ (labelled by {1}) in Figure 9(b) is curious. This is so close to unity that the orientation of the upper and lower region are nearly parallel, making it possible in Figure 9(a) to extrapolate the solution of the upper region, and still remain close to the lower region. In a near parallel case like that it is difficult to pinpoint exactly where the intersection between these regions occurs. This may help to explain why the Eulerian prediction seems to give the concave corner (with a sudden decrease of A in Figure 9(b)) at a different ζ value, closer to the point labelled {2} than {1}: we already know from Figure 8 that $y_{\rm 2nd,cross}$ fits $y_{\rm Eulerian}$ better than $y_{\rm cross}^{\rm inter}$ does. Despite the subtleties, from Figure 9(a) and (b), we see that the current second order solution fits the Eulerian data better than the first order solution does, giving good agreement even up to times of order unity.

9. Conclusions

We have considered a dimensionless form of the pressure-driven growth model used to predict the foam front propagation in an oil reservoir. The front has been captured as the region of finely-textured foam of very low mobility, where injected gas meets reservoir liquid. The foam front is represented as a curve of negligible thickness, which propagates through the porous medium due to the pressure difference across it, and at the same time is retarded by dissipation. The focus here was on early time behaviour, such that the distance the front has propagated horizontally is less than the maximum vertical depth through which it can displace, albeit some of the results we present are extrapolated beyond that regime. As was shown in previous studies [27,32], the foam front can be divided vertically into two regions (lower and upper) that intersect in a concave corner. In this study we have obtained a second order solution in time, to track the trajectory of the material points of the upper region of the front, up to the aforementioned concave corner or matching point between both regions. Obtaining the second order solution in the upper region was particularly challenging owing to strong spatio-temporal non-uniformities that are present there. Our approach was to start with solutions in terms of dimensionless similarity solutions, but then at second order include corrections showing how those similarity solutions break down. This obtained an approximation accurate to order $t^{5/2}$ for the horizontal x location of the material points of the upper region of the front, and an order t^2 accurate approximation for their vertical y location, in each case, with the same order at which the lower region has been computed. At any specified time t, a second order solution predicted the vertical location of the concave corner higher up than the first order solution, but very close to the prediction of an independently obtained Eulerian prediction. We have also proven that initially material points are extracted from the concave corner to populate the lower region, since the topmost point originally present on the front at time $t = 0$ initially moves down faster than the concave corner does, as predicted via the first and/or second order solution obtained in this study. Later on, due to second order effects in time, with the downward motion of such material points slowing down over time, the lower region material points originally on the front eventually reach the concave corner, which must therefore have consumed any previously extracted material points. Therefore, we can assert that all points extracted into the lower region are eventually consumed, however, based on the different approximations that we use, we can actually have different predictions for exactly when this occurs. The issue is that the time we are trying to identify is already sufficiently long that there might be some uncertainty whether expanding in time as far as a second order solution remains adequate or whether yet a higher order correction is required, which will be challenging in view of strong spatio-temporal non-uniformities present

in the upper region. Nevertheless, with the new solutions we were also able to compute the shape of the upper region of the front, which fitted the Eulerian data even up to times of order unity.

Data Accessibility. All results presented here are analytically reproducible, as detailed in the article and in supplementary material.

Authors' Contributions. C.T.-U. carried out the study under P.G.'s supervision. Drafting of the article was shared between C.T.U. and P.G.

Competing Interests. We declare we have no competing interests.

Funding. C.T.-U. received ANID Becas-Chile funding.

References

1. Stevenson P. 2012 *Foam Engineering: Fundamentals and Applications*. John Wiley & Sons.
2. Drenckhan W, Cox S, Delaney G, Holste H, Weaire D, Kern N. 2005 Rheology of ordered foams-on the way to Discrete Microfluidics. *Colloids and Surfaces A: Physicochemical and Engineering Aspects* **263**, 52–64. https://doi.org/10.1016/j.colsurfa.2005.01.005.
3. Kotb MM, Shakiban HK, Sawaby AF. 2013 Foam treatment for varicose veins; efficacy and safety. *Alexandria Journal of Medicine* **49**, 249–253. https://doi.org/10.1016/j.ajme.2012.11.003.
4. Lake LW. 1989 *Enhanced Oil Recovery*. Prentice Hall, Englewood Cliffs, NJ.
5. Shan D, Rossen W. 2004 Optimal injection strategies for foam IOR. *SPE Journal* **9**, 132–150. https://doi.org/10.2118/75180-MS.
6. Wang S, Mulligan CN. 2004 An evaluation of surfactant foam technology in remediation of contaminated soil. *Chemosphere* **57**, 1079–1089. https://doi.org/10.1016/j.chemosphere.2004.08.019.
7. Géraud B, Jones SA, Cantat I, Dollet B, Méheust Y. 2016 The flow of a foam in a two-dimensional porous medium. *Water Resources Research* **52**, 773–790. https://doi.org/10.1002/2015WR017936.
8. Shen X, Zhao L, Ding Y, Liu B, Zeng H, Zhong L, Li X. 2011 Foam, a promising vehicle to deliver nanoparticles for vadose zone remediation. *Journal of Hazardous Materials* **186**, 1773–1780. https://doi.org/10.1016/j.jhazmat.2010.12.071.
9. Zhong L, Szecsody JE, Zhang F, Mattigod SV. 2010 Foam delivery of amendments for vadose zone remediation: propagation performance in unsaturated sediments. *Vadose Zone Journal* **9**, 757–767. https://doi.org/10.2136/vzj2010.0007.
10. Bera A, Ojha K, Mandal A. 2013 Synergistic Effect of Mixed Surfactant Systems on Foam Behavior and Surface Tension. *Journal of Surfactants and Detergents* **16**, 621–630. https://doi.org/10.1007/s11743-012-1422-4.
11. Osei-Bonsu K, Shokri N, Grassia P. 2016 Fundamental investigation of foam flow in a liquid-filled Hele-Shaw cell. *Journal of Colloid and Interface Science* **462**, 288–296. https://doi.org/10.1016/j.jcis.2015.10.017.
12. Kumar S, Mandal A. 2017 Investigation on stabilization of CO2 foam by ionic and nonionic surfactants in presence of different additives for application in enhanced oil recovery. *Applied Surface Science* **420**, 9 – 20. https://doi.org/10.1016/j.apsusc.2017.05.126.
13. Osei-Bonsu K, Grassia P, Shokri N. 2017a Relationship between bulk foam stability, surfactant formulation and oil displacement efficiency in porous media. *Fuel* **203**, 403–410. https://doi.org/10.1016/j.fuel.2017.04.114.
14. Osei-Bonsu K, Grassia P, Shokri N. 2017b Investigation of foam flow in a 3D printed porous medium in the presence of oil. *Journal of Colloid and Interface Science* **490**, 850 – 858. https://doi.org/10.1016/j.jcis.2016.12.015.
15. Grassia P, Mas-Hernández E, Shokri N, Cox S, Mishuris G, Rossen W. 2014 Analysis of a model for foam improved oil recovery. *Journal of Fluid Mechanics* **751**, 346–405. https://doi.org/10.1017/jfm.2014.287.
16. Ma K, Lopez-Salinas JL, Puerto MC, Miller CA, Biswal SL, Hirasaki GJ. 2013 Estimation of Parameters for the Simulation of Foam Flow through Porous Media. Part 1: The Dry-Out Effect. *Energy & Fuels* **27**, 2363–2375. https://doi.org/10.1021/ef302036s.
17. Kovscek AR, Bertin HJ. 2003 Foam mobility in heterogeneous porous media. I. Scaling concepts. *Transport in Porous Media* **52**, 17–35. https://doi.org/10.1023/A:1022312225868.

18. Khatib Z, Hirasaki G, Falls A. 1988 Effects of capillary pressure on coalescence and phase mobilities in foams flowing through porous media. *SPE reservoir engineering* **3**, 919–926. https://doi.org/10.2118/15442-PA.
19. Hirasaki G, Lawson J. 1985 Mechanisms of Foam Flow in Porous Media: Apparent Viscosity in Smooth Capillaries. *Society of Petroleum Engineers Journal* **25**, 176–190. https://doi.org/10.2118/12129-PA.
20. Ma K, Mateen K, Ren G, Luo H, Bourdarot G, Morel D. 2018 Mechanistic Modeling of Foam Flow Through Porous Media in the Presence of Oil: Review of Foam-Oil Interactions and an Improved Bubble Population-Balance Model. *SPE Annual Technical Conference and Exhibition, Dallas, Texas, USA*. https://doi.org/10.2118/191564-MS.
21. Mas-Hernández E, Grassia P, Shokri N. 2015 Foam improved oil recovery: Foam front displacement in the presence of slumping. *Colloids and Surfaces A: Physicochemical and Engineering Aspects* **473**, 123–132. https://doi.org/10.1016/j.colsurfa.2014.12.023.
22. Ma K, Ren G, Mateen K, Morel D, Cordelier P. 2015 Modeling techniques for foam flow in porous media. *SPE Journal* **20**, 453–470. https://doi.org/10.2118/169104-PA.
23. Eneotu M, Grassia P. 2020 Modelling foam improved oil recovery: towards a formulation of pressure-driven growth with flow reversal. *Proceedings of the Royal Society A: Mathematical, Physical and Engineering Sciences* **476**, 2020–0573. https://doi.org/10.1098/rspa.2020.0573.
24. Kovscek A, Patzek T, Radke C. 1995 A mechanistic population balance model for transient and steady-state foam flow in Boise sandstone. *Chemical Engineering Science* **50**, 3783–3799. https://doi.org/10.1023/A:1010740811277.
25. Falls A, Hirasaki G, Patzek Tea, Gauglitz D, Miller D, Ratulowski T. 1988 Development of a mechanistic foam simulator: the population balance and generation by snap-off. *SPE reservoir engineering* **3**, 884–892. https://doi.org/10.2118/14961-PA.
26. Farajzadeh R, Andrianov A, Krastev R, Hirasaki G, Rossen W. 2012 Foam–oil interaction in porous media: Implications for foam assisted enhanced oil recovery. *Advances in Colloid and Interface Science* **183-184**, 1–13. https://doi.org/10.1016/j.cis.2012.07.002.
27. Grassia P, Lue L, Torres-Ulloa C, Berres S. 2017 Foam front advance during improved oil recovery: Similarity solutions at early times near the top of the front. *Journal of Fluid Mechanics* **828**, 527–572. https://doi.org/10.1017/jfm.2017.541.
28. Salazar Castillo RO, Ter Haar SF, Ponners CG, Bos M, Rossen W. 2020 Fractional-Flow Theory for Non-Newtonian Surfactant-Alternating-Gas Foam Processes. *Transport in Porous Media* **131**, 399–426. https://doi.org/10.1007/s11242-019-01351-6.
29. Kovscek AR, Patzek TW, Radke CJ. 1997 Mechanistic foam flow simulation in heterogeneous and multidimensional porous media. *SPE Journal* **2**, 511–526. https://doi.org/10.2118/39102-PA.
30. Zeng Y, Muthuswamy A, Ma K, Wang L, Farajzadeh R, Puerto M, Vincent-Bonnieu S, Eftekhari AA, Wang Y, Da C, Joyce JC, Biswal SL, Hirasaki GJ. 2016 Insights on foam transport from a texture-implicit local-equilibrium model with an improved parameter estimation algorithm. *Industrial and Engineering Chemistry Research* **55**, 7819–7829. doi.org/10.1021/acs.iecr.6b01424.
31. Mas Hernández E, Grassia P, Shokri N. 2016 Modelling foam improved oil recovery within a heterogeneous reservoir. *Colloids and Surfaces A: Physicochemical and Engineering Aspects* **510**, 43–52. https://10.1016/j.colsurfa.2016.07.064.
32. Torres-Ulloa C, Berres S, Grassia P. 2018 Foam-liquid front motion in Eulerian coordinates. *Proceedings of the Royal Society A: Mathematical, Physical and Engineering Sciences* **474**, 2018–0290. https://doi.org/10.1098/rspa.2018.0290.
33. Kurganov A, Noelle S, Petrova G. 2001 Semidiscrete central-upwind schemes for hyperbolic conservation laws and Hamilton–Jacobi equations. *SIAM Journal on Scientific Computing* **23**, 707–740. https://doi.org/10.1137/S1064827500373413.
34. Osher S, Fedkiw R. 2006 *Level Set Methods and Dynamic Implicit Surfaces*. Springer. https://doi.org/10.1007/b98879.
35. Grassia P, Torres-Ulloa C, Berres S, Mas-Hernández E, Shokri N. 2016 Foam front propagation in anisotropic oil reservoirs. *European Physical Journal E* **39:42**. https://doi.org/10.1140/epje/i2016-16042-5.
36. de Velde Harsenhorst R, Dharma A, Andrianov A, Rossen W. 2014 Extension of a simple model for vertical sweep in foam SAG displacements. *SPE Reservoir Evaluation & Engineering* **17**, 373–383. https://doi.org/10.2118/164891-PA.

37. Chan TF, Vese LA. 2001 Active contours without edges. *IEEE Transactions on Image Processing* **10**, 266–277. https://doi.org/10.1109/83.902291.

PROCEEDINGS A

rspa.royalsocietypublishing.org

Review

Article submitted to journal

Subject Areas:
Fluid mechanics, Applied mathematics, Chemical engineering

Keywords:
pressure-driven growth model, foams, front propagation, porous media, Taylor expansion

Author for correspondence:
C. Torres-Ulloa
e-mail:
carlos.torres-ulloa@strath.ac.uk
carlos.torres@uct.cl

THE ROYAL SOCIETY
PUBLISHING

Supplementary material: "Breakdown of similarity solutions: A perturbation approach for front propagation during foam improved oil recovery"

C. Torres-Ulloa[1,2] & P. Grassia[1]

[1]Department of Chemical and Process Engineering, University of Strathclyde, James Weir Building, 75 Montrose St, Glasgow G1 1XJ, UK.
[2] Departamento de Procesos Industriales, Facultad de Ingeniería, Universidad Católica de Temuco, Av. Rudecindo Ortega 02950, Temuco, Chile.

Summary: This supplementary material begins by reviewing and analysing first order early-time similarity solutions (sections S 1–S 2), specifically in the context of the upper region of a foam front that is propagating during foam improved oil recovery. These first order solutions, applicable in the limit of early times, were obtained in prior work by [1], and the discussion given below expands upon that in the main text presented within sections 3–4 After that, the focus switches to second order accurate solutions in time which is the novel contribution of the present work. We now consider both the lower (section S 3) and the upper (sections S 4–S 5) regions of a propagating foam front. The analysis for the lower region (section S 3) proves relatively straightforward. However, since strong spatio-temporal non-uniformities are present in the upper region of the front, obtaining second order solutions there is challenging: the procedure is detailed in section S 4, feeding into the results of section S 5. The key results we deduce are given in sections S 3 and S 5, specifically by equation (S 3.7) (lower region), and by equations (S 5.2), (S 5.3) and (S 5.4) (upper region). In section S 6, we plot the difference between solutions in the upper and lower regions to identify where these regions match: this expands on the methodology outlined in section 5(d) of the main text. Section S 7 gives expressions for front orientation angle, vertical coordinate and horizontal coordinate on time, specifically at the matching point between upper and lower regions: this supports the discussion of sections 6–7 in the main text. In section S 8 we track material points in the

lower region in an analogous fashion to the way we already track material points the upper region: this corresponds to an alternative methodology also mentioned in section 5(d) with data presented in section 7. Finally, in section S 9 we obtain a set of equations used to extrapolate the second order solution to a wider domain, beyond the domain where it was originally obtained: this supports the discussion of section 8 in the main text.

S 1. Review of first order similarity equations

As established in [1], the front upper region can be expressed in terms of a set of similarity variables. These variables as given in the main text are: A as the rescaled front orientation angle, ζ as the rescaled vertical front location, and Ξ as the rescaled horizontal front displacement. In [1] it was proven that it is possible to obtain a leading order expression to define ζ as a function of A, as

$$\mathrm{d}\zeta/\mathrm{d}A = (1-(1-cA)^{1/c-1})/(1-c), \tag{S 1.1}$$

which after integrating gives

$$\zeta = ((1-c)-(1-cA)+c(1-cA)^{1/c})/(c(1-c)), \tag{S 1.2}$$

where $2c-1$ is the assumed invariant ratio between $\mathrm{d}s/\mathrm{d}y$ and $\mathrm{d}x/\mathrm{d}y$, over the upper region. As proven in [1], choosing $c=3/4$ and hence $2c-1=1/2$, gives a suitable approximation for it. In [1] it was demonstrated, via a far more complex integro-differential formulation of the system of equations, that the ratio between $\mathrm{d}s/\mathrm{d}y$ and $\mathrm{d}x/\mathrm{d}y$ in the upper region always lay between 0.5 and 0.51. Hence, treating it as invariant (with assumed value 0.5), despite being an ad hoc approximation led to negligible error, and had the advantage of producing the simple analytical form, given by equation (S 1.2).

To determine the horizontal displacement of the upper region of the front, we need to obtain an approximation for Ξ. As in [1], we can take a first order Taylor expansion of $\tan(\alpha)$ and insert it into equation (2.6) (given in the main text), in order to obtain for $y \geq 1-(t/2)\zeta_{\mathrm{cross}}$, i.e. $\zeta \leq \zeta_{\mathrm{cross}}$ (upper region), that

$$\Xi \approx \frac{1}{2\sqrt{2}}\int_0^{\zeta} A\,\mathrm{d}\zeta = \frac{1}{2\sqrt{2}}\int_0^{A} A\frac{\mathrm{d}\zeta}{\mathrm{d}A}\,\mathrm{d}A = \frac{2(1+A)(1-cA)^{1/c}+A^2(1+c)-2}{4\sqrt{2}(1-c^2)}, \tag{S 1.3}$$

where equations (2.4), (2.7), (3.1) (as given in the main text) and (S 1.1) have been used.

Here we have introduced two similarity equations ((S 1.2) and (S 1.3)) to compute the upper region of the front in terms of a rescaled in time front orientation angle A. Therefore, each point on the upper region of the front must have a well defined A value, which governs on its current ζ and Ξ location. These were the forms of the similarity equations originally obtained by [1]. In section 3 of the main text however we expressed these solutions in terms of an alternative, more convenient variable ψ (the fraction of total time that an injected material point has been on the front). The expressions in terms of ψ however are equivalent to those written in terms of A.

S 2. Analysing first order similarity solution

As in [1], we have computed the upper region of the front in terms of ψ via a first order solution (see sections 3–4 in the main text), up to ψ_{cross}, where the matching point between the lower and upper region of the front is located. The lower region at first order is given in section 2 in the main text. At leading order we have obtained that $\psi_{\mathrm{cross}} \approx 0.9431$, with $\zeta_{\mathrm{cross}} \approx 0.9397$, and $\Xi_{\mathrm{cross}} \approx 0.2733$. Even on the basis of these first order results, we can establish a number of useful concepts, which are highlighted below. We can determine for instance, out of all the material points currently on the front, a minimum injected time $t_{\mathrm{inj(min)}}$, which corresponds to the time at which a material point that has reached the concave corner was injected. This is explained in detail in section (a). On the other hand, there is also a maximum survival time that a material point can remain on the upper region. This is explained in detail in section (b). Then, in section (c) we show how to rescale

the vertical coordinated ζ as a function of ψ, so as to be able to track more readily the location of different injected material points, as explained in section (d). All of these concepts carry over to our second order analysis so we make extensive use of them in the main text (see e.g. the results presented in section 7 in the main text).

(a) Minimum injected time $t_{\mathrm{inj(min)}}$ as a function of time t

Since $\psi_{\mathrm{cross}} < 1$, it follows from equation (3.2) that the point injected at $t_{\mathrm{inj}} = 0$ has been already consumed or destroyed by the concave corner. This then implies that (for any given t) there is a minimum time ($t_{\mathrm{inj(min)}}$) at which a still surviving material point has been injected without yet having been destroyed by the kink, so we can establish that $t_{\mathrm{inj}} \in [t_{\mathrm{inj(min)}}, t]$ defines the full set of material points on the front. At any time t, there must be a material point in the upper region just beside the concave corner, which was injected at a time $t_{\mathrm{inj(min)}}$ significantly less than t, with

$$t_{\mathrm{inj(min)}} = (1 - \psi_{\mathrm{cross}})\, t. \tag{S 2.1}$$

If ψ_{cross} is found via the first order matching point, we can estimate for any small time t that $t_{\mathrm{inj(min)}} \approx 0.0569\, t$, implying that the points injected before such time have already been consumed by the concave corner. This expression is perturbed when second order corrections are included (equation (7.2) in the main text).

(b) Maximum survival time t_{max} as a function of time t_{inj}

We can also consider that each injected material point in the front, has a maximum survival time (t_{max} depending on t_{inj}), which is the estimated time that a material point can survive before reaching the kink or matching point [1] i.e. before being consumed by the concave corner. Note that $t_{\mathrm{max}}(t_{\mathrm{inj}})$ is the inverse of $t_{\mathrm{inj(min)}}(t)$. Hence

$$t_{\mathrm{max}} = t_{\mathrm{inj}}/(1 - \psi_{\mathrm{cross}}). \tag{S 2.2}$$

Note that for $\psi_{\mathrm{cross}} \approx 0.9431$ (the leading order result), it follows $t_{\mathrm{max}} = 17.57 t_{\mathrm{inj}}$. At second order, equation (7.1) applies instead. By definition, for $t_{\mathrm{inj}} = t_{\mathrm{inj(min)}}$, we find $t_{\mathrm{max}} = t$. Hence, we can then determine that for any given t_{inj}, the domain of t values of interest will be $t_{\mathrm{inj}} \le t \le t_{\mathrm{max}}$, and consequently $1 \le t/t_{\mathrm{inj}} \le t_{\mathrm{max}}/t_{\mathrm{inj}}$. This is the domain plotted in Figure 3(b) in the main text.

(c) Rescaled ζ_+ as a function of ψ

Since vertical coordinate ζ has been computed for the upper region at leading order in equation (3.4) (as a function of ψ up to ψ_{cross}), we can calculate at any time t, the position $\zeta(\psi)$ of the material points injected at different $t_{\mathrm{inj}} \in [t_{\mathrm{inj(min)}}, t]$. However, we can also follow the trajectory of a single material point within the upper region, by fixing t_{inj} and varying ψ, which corresponds to tracking the point's position over time t. Hence, we define $\zeta_+ = (1 - y)/(t_{\mathrm{inj}}/2)$ as the rescaled vertical position of a material point. Here, ζ_+ is a direct measure of $1 - y$, since t_{inj} is fixed for each material point. By contrast, for $\zeta = (1 - y)/(t/2)$ the relationship is less straightforward since both $1 - y$ and t change following the material point. Now consider this material point injected at time t_{inj} which is currently (at some time t, and hence at some $\psi = 1 - t_{\mathrm{inj}}/t$) at a vertical location $\zeta_+(\psi) \equiv \zeta(\psi)/(1 - \psi)$. It is of interest to ask where is the location of the concave corner relative to this point. This is always at $\zeta = \zeta_{\mathrm{cross}}$ (for a well defined value of ζ_{cross}, e.g. at leading order $\zeta_{\mathrm{cross}} \approx 0.9397$), and hence at $\zeta_+ = \zeta_{\mathrm{cross}}/(1 - \psi)$. This gives the instantaneous location of the cross-over point, even though the material point of interest has not yet reached it. Likewise, we can track the position of a lower region material point originally (at $t = 0$) at the top of the front, by considering that this point follows a trajectory $\zeta = 1$, which follows from a first order approximation to the lower region (see equation (2.3)), implying that at first order $\zeta_+ \equiv 1/(1 - \psi)$. Thus, we have distinct formulae (plotted at leading order in Figure 3(b) in the main text), respectively for a material point in the upper region, for the concave corner or kink, and for a material point in the lower region.

Generalisations to these relations at second order are possible, see e.g. equations (5.6), (S 7.6) and (S 8.10).

(d) Using ζ_+ vs ψ to compare trajectories

Figure 3(b) in the main text, which is a first order approximation in the limit of arbitrary small $t_{\rm inj}$ and hence arbitrary small t with $t_{\rm inj} \le t \le t_{\rm inj}/(1-\psi_{\rm cross})$, shows how a point originally at the top of the lower region $y_0 = 1$ moves downwards with a velocity of $-1/2$ (or equivalently retains $\zeta = 1$ for all time), which is represented in terms of ζ_+ as $1/(1-\psi)$ (dash-dotted line). Here we see that a gap is present even at $\psi = \psi_{\rm cross}$, between this uppermost material point originally on the front, and the final position of the material point injected at $t_{\rm inj}$, which coincides with the concave corner (specifically when $\psi = \psi_{\rm cross}$). The existence of this gap implies that material points must have been extracted from the kink or concave corner to populate the lower region. This however, is a first order theory, that must be perturbed at second order. We know the second order correction to the lower region's material points (equation (2.11)), and we have also mentioned that the point originally at the top of the front moves downwards (considering the second order effect via equation (2.12)) slower than it would do for the leading order term in equation (2.3). Nevertheless, this in itself does not tell us if the topmost point originally on the front moves upwards sufficiently (relative to its first order location) so as to overtake the position of the concave corner. To address this question we need to have a second order approximation for the position of the concave corner. Only when that second approximation is available can we determine whether material points in the lower region initially extracted from the kink are subsequently consumed by it. However, given the corner is where the upper and lower regions match, we can only start to answer this question if we also have a second order approximation to the upper region: this then is what the main text develops.

In summary, employing the first order solution we were able to determine the matching point between the upper and the lower region of the front for $t \ll 1$ or equivalently $t_{\rm inj} \ll 1$, by using similarity variables. We can also verify the existence of the concave corner at the matching point, which was proven by [1]. Since rescaled orientation angle $A_{\rm cross}$ in the upper region (see value $A_{\rm cross,0}$ in Table 1) is greater than unity (which is the analogous amount that the lower region reorients near the top at small times), the front not only curves sharply in the upper region, but also undergoes an abrupt reorientation at a concave corner in order to meet the lower region. We also demonstrated that material points are extracted from the concave corner in order to populate the lower region (at least in the limit of small times), and that material points in the upper region are being destroyed at the matching point. However, even though we are studying an arbitrarily small interval of time $t_{\rm inj} \le t \le t_{\rm inj}/(1-\psi_{\rm cross}) = t_{\rm max}$, with $t_{\rm inj} \ll 1$, the motion of material points (ζ_+ vs $t/t_{\rm inj}$) in the upper region, as shown in Figure 3(b), is non-uniform over this interval. These strong non-uniformities in space and time make it challenging to perturb the upper region to higher orders of accuracy (in contrast to the lower region in which all points move down uniformly with velocity $-1/2$ at leading order via equation (2.3)). In the main text (section 5 onwards) however, we tackle that challenge to determine how the upper region solution is perturbed as t increases, and thereby obtain a corresponding second order solution for the location of the matching point, taking proper account of the spatio-temporal non-uniformities that are present.

S 3. Correction to ξ at order $t^{5/2}$ for lower region front shape

Previous work [1], derived a so called improved Velde solution for x vs y and t, in the lower region (equation (2.1) in the main text), that was accurate through order $t^{3/2}$ in time. However, in the present work we have points in the upper region placed horizontally to order t accuracy in Ξ, hence order $t^{5/2}$ accuracy in ξ (since $\xi \equiv \Xi\, t^{3/2}$ with $x \equiv \sqrt{2t} - \xi$). We therefore need further improvement in the description of the lower region, to be consistent between both regions. Hence, what we seek for the lower region, is to incorporate an order $t^{5/2}$ correction to the horizontal x location, alongside an order t^2 correction to the vertical location y of the material points, the latter being already available as given by equation (2.11). This is achieved in what follows via an order t correction to the variable

Ξ in the lower region. We start by considering the motion of a Lagrangian material point in the x direction, which is given by equation (1.3), as

$$\mathrm{d}x^2/\mathrm{d}t \approx 2\, y(y_0,t)\, \cos(\alpha)\, (x/s), \tag{S 3.1}$$

where α denotes the orientation angle of the front normal relative to the horizontal, s denotes the path length that a lower region material point has displaced, and y_0 denotes the initial vertical location of a material point in the lower region, which moves to a location $y(y_0,t)$ at time t. At early times near the top of the lower region, we can set $y_0 = 1-\mathfrak{z}_0$, where it turns out $\mathfrak{z}_0 \ll 1$ for the material points of interest. Here at early times, any value of $\mathfrak{z}_0$ of interest can be treated as a quantity of order t, since via equations (2.4) and (2.11), we can compute $y \approx 1-\mathfrak{z}_0 - t/2 + (5t^2)/48$, but also $\zeta \equiv (1-y)/(t/2)$, and hence

$$\mathfrak{z}_0 \approx (\zeta-1)(t/2) + 5t^2/48. \tag{S 3.2}$$

Equation (S 3.2) implies that if we focus attention near the top of the lower region where $\zeta - 1$ is at most order unity, then $\mathfrak{z}_0$ values of interest are at most order t. Within equation (S 3.1), since α can be expressed geometrically as $\alpha = \mathrm{atan}(\mathrm{d}x/\mathrm{d}y)$, we can obtain via Taylor expansion that $\cos(\alpha) \approx 1 - (1/2)(\mathrm{d}x/\mathrm{d}y)^2 + (3/8)(\mathrm{d}x/\mathrm{d}y)^4$, where $(\mathrm{d}x/\mathrm{d}y)^2$ is computed using the improved Velde solution (given by equation (2.1)), but now written in terms of $\mathfrak{z}_0$ and t, i.e. by using

$$x \approx \sqrt{2t - 2\mathfrak{z}_0 t - 5t^2/6}, \tag{S 3.3}$$

in which y has been replaced by $y \approx 1-\mathfrak{z}_0 - t/2$, via first order approximation, which is given by equation (2.2). Consistent with the current order of expansion, $(\mathrm{d}x/\mathrm{d}y)^4$ is calculated using the Velde solution ($x \approx \sqrt{2yt}$). Then, we compute x/s by considering that $\mathrm{d}s/\mathrm{d}t = \sqrt{(\mathrm{d}x/\mathrm{d}t)^2 + (\mathrm{d}y/\mathrm{d}t)^2}$, which after Taylor expanding to terms of fourth power, gives

$$s \approx x + \frac{1}{2}\int_0^t \frac{(\mathrm{d}y/\mathrm{d}t')^2}{\mathrm{d}x/\mathrm{d}t'}\,\mathrm{d}t' - \frac{1}{8}\int_0^t \frac{(\mathrm{d}y/\mathrm{d}t')^4}{(\mathrm{d}x/\mathrm{d}t')^3}\,\mathrm{d}t', \tag{S 3.4}$$

with t' here being a dummy integration variable. Here $\mathrm{d}y/\mathrm{d}t'$ is calculated using equation (2.11), $\mathrm{d}x/\mathrm{d}t'$ uses equation (S 3.3), and $(\mathrm{d}x/\mathrm{d}t')^3$ uses the Velde solution. Hence, we can express equation (S 3.1), by Taylor expanding out to order t^2 terms (treating $\mathfrak{z}_0$ itself as being order t), as

$$\begin{aligned}\frac{\mathrm{d}x^2}{\mathrm{d}t} &\approx 2\left(1-\mathfrak{z}_0-\frac{t}{2}+\frac{5t^2}{48}\right)\left(1-\frac{t}{4}\left(1+\mathfrak{z}_0+\frac{t}{24}\right)\right)\left(1-\frac{t}{12}\left(1+\mathfrak{z}_0+\frac{t}{120}\right)\right)\\ &\approx 2 - 2\mathfrak{z}_0 - \frac{5t}{3} + \frac{101t^2}{180}.\end{aligned} \tag{S 3.5}$$

Next, integrating (S 3.5), retaining terms up to third power in time, we deduce

$$x \approx \sqrt{2t - 2\mathfrak{z}_0 t - 5t^2/6 + 101t^3/540}. \tag{S 3.6}$$

Then, and analogously to equation (2.8), we can obtain

$$\xi = \frac{2t-x^2}{\sqrt{2t}+x} \approx \frac{2\mathfrak{z}_0 t + 5t^2/6 - 101t^3/540}{\sqrt{2t}+\sqrt{2t-2t\mathfrak{z}_0 - 5t^2/6}}. \tag{S 3.7}$$

Here, we do not need a high accuracy approximation to x in the denominator, so we have substituted from (S 3.3). Finally, Taylor expanding in t up to second order, and introducing equation (S 3.2), we can compute $\Xi = \xi/t^{3/2}$ as defined by equation (2.7). The resulting equation we obtain is (see equation (5.4) in the main text)

$$\Xi \approx \frac{1}{2\sqrt{2}}\left(\zeta - \frac{1}{6} + \frac{t}{8}\left(\zeta^2 - \frac{\zeta}{3} + \frac{107}{540}\right)\right), \tag{S 3.8}$$

which represents an improvement upon equation (2.9) including a correction term for small but finite t.

S 4. Order t correction to upper region rescaled variables A, ζ and Ξ

To determine with second order accuracy, the front orientation angle α, the vertical location y, and horizontal location x of points in the upper region, we need to compute (in terms of the parameter ψ, i.e. the fraction of time a material point has been on the front) the functions $A_1(\psi)$, $\zeta_1(\psi)$ and $\Xi_1(\psi)$, respectively. These are required to compute perturbations to rescaled angle A, rescaled vertical coordinate ζ and rescaled horizontal coordinate ξ via equations (5.1)–(5.3) in the main text. The key results we deduce here are equations (S 4.15), (S 4.24) and (S 4.26), which are used to compute $A_1(\psi)$, $\zeta_1(\psi)$ and $\Xi_1(\psi)$, respectively, the actual functional forms then being obtained in equations (S 5.2), (S 5.3) and (S 5.4) (see section S 5 to follow). We compute these actual functional forms by fixing a parameter $c = 3/4$, as was established in section 3 in the main text and in section S 1 following the recommendation of [1]. Results are plotted in Figure 1 (see section S 5). Note that $A_1(\psi)$, $\zeta_1(\psi)$ and $\Xi_1(\psi)$ are all negative and become increasingly negative as ψ increases. It follows that for a given ψ, equations (5.1)–(5.3) predict a front shape that reorients less and displaces less vertically and horizontally than the corresponding first order prediction.

(a) Correction at order t for upper region front reorientation angle $A(\psi, t)$

We start by considering that the variation of the angle α (front normal relative to the horizontal) with time t, of a Lagrangian film element can be quantified in terms of the variation in the normal velocity of the front along an element $\mathcal{S}$ (distance measured along the front itself), as follows

$$\left(\frac{\mathrm{d}\alpha}{\mathrm{d}t}\right)_L = -\frac{\mathrm{d}}{\mathrm{d}\mathcal{S}}\left(\frac{y}{s}\right), \tag{S 4.1}$$

where y/s is the material point speed given by equation (1.1), and where the subscript L reminds us that we are dealing with a Lagrangian material point. Here $\mathcal{S}$ is specifically distance along the front measured downward (see Figure 1 in the main text); this is not to be confused with s which is the material point trajectory. We can differentiate equation (S 4.1) to obtain

$$\left(\frac{\mathrm{d}\alpha}{\mathrm{d}t}\right)_L = -\frac{1}{s}\frac{\mathrm{d}y}{\mathrm{d}\mathcal{S}} + \frac{y}{s^2}\frac{\mathrm{d}s}{\mathrm{d}y}\frac{\mathrm{d}y}{\mathrm{d}\mathcal{S}} = \frac{\cos(\alpha)}{s}\left(1 - \frac{y}{s}\frac{\mathrm{d}s}{\mathrm{d}y}\right), \tag{S 4.2}$$

where, $\cos(\alpha) = -\mathrm{d}y/\mathrm{d}\mathcal{S}$ (by geometric definition). We can express s in terms of x by assuming that, in the upper region, the ratio between $\mathrm{d}s/\mathrm{d}y$ and $\mathrm{d}x/\mathrm{d}y$ (these derivatives being measured along the front) can be assumed invariant and equal to $2c-1$ (the reasons for making this assumption are discussed in section S 1 and justified in [1]). Therefore, imposing a condition (as in the main text) that the leading edge of the front is at location $\sqrt{2t}$ with s and x being equal at that point, we can express (moving down from the leading edge)

$$s \approx \sqrt{2t} - (2c-1)(\sqrt{2t} - x) \approx \sqrt{2t} - (2c-1)\xi, \tag{S 4.3}$$

where ξ is the horizontal displacement of the front, from the leading edge $\sqrt{2t}$ to a point x on the front, as per equation (2.5). Replacing $\mathrm{d}s/\mathrm{d}y$ by $(2c-1)\mathrm{d}x/\mathrm{d}y$ (the assumed invariant ratio alluded to earlier), we obtain

$$\left(\frac{\mathrm{d}\alpha}{\mathrm{d}t}\right)_L \approx \frac{\cos(\alpha)}{\sqrt{2t} - (2c-1)(\sqrt{2t} - x)}\left(1 - \frac{(2c-1)\,y}{\sqrt{2t} - (2c-1)(\sqrt{2t} - x)}\frac{\mathrm{d}x}{\mathrm{d}y}\right). \tag{S 4.4}$$

Here, since $\mathrm{d}x/\mathrm{d}y = \tan(\alpha)$ (by geometry), we can approximate $\mathrm{d}x/\mathrm{d}y \approx (\alpha + \alpha^3/3)$ which is obtained via Taylor expansion in powers of α. We can also Taylor expand $\cos(\alpha)$ in powers of

α, and thereby we deduce

$$\left(\frac{\mathrm{d}\alpha}{\mathrm{d}t}\right)_L \approx \frac{\left(1-\frac{\alpha^2}{2}\right)}{\sqrt{2t}-(2c-1)(\sqrt{2t}-x)}\left(1-\frac{(2c-1)\,y}{\sqrt{2t}-(2c-1)(\sqrt{2t}-x)}\left(\alpha+\frac{\alpha^3}{3}\right)\right). \quad \text{(S 4.5)}$$

Now, introducing $\xi=\sqrt{2t}-x$, along with similarity variables $\alpha=\sqrt{t/2}\,A$, $\zeta=(1-y)/(t/2)$, and $\xi=t^{3/2}\Xi$, we can determine

$$\left(\frac{\mathrm{d}\alpha}{\mathrm{d}t}\right)_L \approx \frac{1}{\sqrt{2t}}\left(\frac{\left(1-\frac{tA^2}{4}\right)}{1-\frac{(2c-1)}{\sqrt{2}}t\Xi}\left(1-\frac{A}{2}\left(\frac{(2c-1)\left(1-\frac{t}{2}\zeta\right)}{1-\frac{(2c-1)}{\sqrt{2}}t\Xi}\right)\right)\left(1+\frac{tA^2}{6}\right)\right). \quad \text{(S 4.6)}$$

We now assume $t\ll 1$, and Taylor expanding each factor in the parentheses in terms of small parameters, we end up with an expression that has a leading order term plus an order t correction, plus higher order terms that we neglect. We obtain

$$\left(\frac{\mathrm{d}\alpha}{\mathrm{d}t}\right)_L \approx \frac{1}{\sqrt{2t}}\left(1-\frac{A(2c-1)}{2}\right.$$
$$\left.+t\left(-\frac{A_0^2}{4}-\frac{A_0^3(2c-1)}{12}+\frac{(2c-1)A_0\zeta_0}{4}+\left(\frac{2c-1}{\sqrt{2}}-\frac{A_0(2c-1)^2}{2\sqrt{2}}\right)\Xi_0\right)\right), \quad \text{(S 4.7)}$$

where terms appearing on the right hand side at order t, such as the orientation angle A, the front vertical location ζ and the front horizontal displacement Ξ, have been replaced by leading order expressions $A_0(\psi)$, $\zeta_0(\psi)$ and $\Xi_0(\psi)$, given by equations (3.3), (3.4) and (3.5), respectively. Thus, we express (S 4.7) as

$$\left(\frac{\mathrm{d}\alpha}{\mathrm{d}t}\right)_L \approx \frac{1}{\sqrt{2t}}\left(1-\frac{A(2c-1)}{2}+t\,\Omega(A_0,\zeta_0,\Xi_0)\right), \quad \text{(S 4.8)}$$

where $\Omega(A_0,\zeta_0,\Xi_0)$ corresponds to

$$\Omega(A_0,\zeta_0,\Xi_0)=-\frac{A_0^2}{4}-\frac{A_0^3(2c-1)}{12}+\frac{(2c-1)A_0\zeta_0}{4}+\left(\frac{2c-1}{\sqrt{2}}-\frac{A_0(2c-1)^2}{2\sqrt{2}}\right)\Xi_0. \quad \text{(S 4.9)}$$

Since A_0, ζ_0 and Ξ_0 are well defined functions of ψ (see equations (3.3)–(3.5) in the main text), we can express $\Omega\equiv\Omega(\psi)$, the result being given by equation (S 5.1) in section S 5. We can also compute $(\mathrm{d}\alpha/\mathrm{d}t)_L$ as a function of A and ψ, by using the similarity equations (3.1) and (3.2). Then, we can express the left side hand of equation (S 4.8), using equation (5.1), as follows

$$\left(\frac{\mathrm{d}\alpha}{\mathrm{d}t}\right)_L \approx \frac{1}{2\sqrt{2t}}(A_0+t\,A_1)+\sqrt{\frac{t}{2}}\left(\left(\frac{\mathrm{d}A_0}{\mathrm{d}\psi}\right)\left(\frac{\mathrm{d}\psi}{\mathrm{d}t}\right)_L+A_1+t\left(\frac{\mathrm{d}A_1}{\mathrm{d}\psi}\right)\left(\frac{\mathrm{d}\psi}{\mathrm{d}t}\right)_L\right), \quad \text{(S 4.10)}$$

where since $\psi=(1-t_{\mathrm{inj}}/t)$ (which is given by equation (3.2)), we can determine

$$(\mathrm{d}\psi/\mathrm{d}t)_L=(1-\psi)/t. \quad \text{(S 4.11)}$$

Combining equations (S 4.8) and (S 4.10), and matching terms at each order of t, we find

$$(1-\psi)(\mathrm{d}A_0/\mathrm{d}\psi)=1-cA_0, \quad \text{(S 4.12)}$$

and

$$A_1(1+c)+(1-\psi)(\mathrm{d}A_1/\mathrm{d}\psi)=\Omega(\psi). \quad \text{(S 4.13)}$$

Hence, we can compute

$$A_0=(1-(1-\psi)^c)/c, \quad \text{(S 4.14)}$$

which corresponds to the leading order front reorientation A_0, obtained in equation (3.3). Moreover, applying the integrating factor $(1-\psi)^{-(1+c)}$ to equation (S 4.13), we deduce

$$A_1 = (1-\psi)^{1+c}\int_0^{\psi}\frac{\Omega(\psi')}{(1-\psi')^{2+c}}\,\mathrm{d}\psi', \tag{S 4.15}$$

ψ' here being a dummy integration variable. Then, after substituting from equation (S 5.1) (given in section S 5) and integrating, we obtain an explicit expression for $A_1 \equiv A_1(\psi)$, given by equation (S 5.2), in section S 5. Hence we have obtained the order t correction, to compute the front orientation A. This equation will be used in what follows, to determine the order t term contributing to the vertical location of the upper region's material points.

(b) Correction at order t for upper region front vertical location $\zeta(\psi, t)$

We start by considering the velocity of a Lagrangian material point in the y direction, given by equation (1.2) [1]. Then, Taylor expanding $\sin(\alpha)$ in terms of the small angle α, and rewriting (1.2) we obtain

$$\left(\frac{\mathrm{d}y}{\mathrm{d}t}\right)_L \approx \frac{-(1-(1-y))\left(\alpha-\frac{\alpha^3}{6}\right)}{\sqrt{2t}-(\sqrt{2t}-s)} \approx -\frac{\alpha}{\sqrt{2t}}\left(1-(1-y)-\frac{\alpha^2}{6}+\frac{(2c-1)}{\sqrt{2t}}\xi\right), \tag{S 4.16}$$

where we have substituted equation (S 4.3) into (S 4.16), and Taylor expanded.
Now introducing the similarity equations (2.4), (2.7) and (3.1), we can express $\alpha = \sqrt{t/2}\,A$, $\zeta = (1-y)/(t/2)$, and $\xi = t^{3/2}\Xi$, respectively, in order to obtain

$$\zeta + t\left(\frac{\mathrm{d}\zeta}{\mathrm{d}t}\right)_L \approx A\left(1 - t\frac{\zeta}{2} - t\frac{A^2}{12} + t\frac{(2c-1)}{\sqrt{2}}\Xi\right), \tag{S 4.17}$$

where we can approximate the front orientation as $A \approx A_0 + tA_1$, so we can compute

$$\zeta + t\left(\frac{\mathrm{d}\zeta}{\mathrm{d}t}\right)_L \approx A_0 + tA_1 - t\frac{A_0\zeta_0}{2} - t\frac{A_0^3}{12} + t\frac{(2c-1)}{\sqrt{2}}A_0\Xi_0. \tag{S 4.18}$$

In going from equation (S 4.17) to (S 4.18), terms appearing on the right side hand at order t, such as the orientation angle A, the front vertical location ζ and the front horizontal displacement Ξ, have been replaced by $A_0(\psi)$, $\zeta_0(\psi)$ and $\Xi_0(\psi)$, given by equations (3.3), (3.4) and (3.5). Moreover, using equation (5.2), we compute the left hand side of equation (S 4.18) as follows

$$\zeta + t\,(\mathrm{d}\zeta/\mathrm{d}t)_L \approx \zeta_0 + t\,(\mathrm{d}\zeta_0/\mathrm{d}\psi)\,(\mathrm{d}\psi/\mathrm{d}t)_L + 2t\,\zeta_1 + t^2\,(\mathrm{d}\zeta_1/\mathrm{d}\psi)\,(\mathrm{d}\psi/\mathrm{d}t)_L\,, \tag{S 4.19}$$

where $(\mathrm{d}\psi/\mathrm{d}t)_L$ is given by equation (S 4.11), in order to obtain

$$\zeta + t\,(\mathrm{d}\zeta/\mathrm{d}t)_L \approx \zeta_0 + (1-\psi)\,(\mathrm{d}\zeta_0/\mathrm{d}\psi) + 2t\,\zeta_1 + t(1-\psi)\,(\mathrm{d}\zeta_1/\mathrm{d}\psi)\,. \tag{S 4.20}$$

Here, $\mathrm{d}\zeta_0/\mathrm{d}\psi$ and $\mathrm{d}\zeta_1/\mathrm{d}\psi$ are well defined, as ζ_0 and ζ_1 depend only on ψ. Then, from combining equations (S 4.18) and(S 4.20), and matching terms at each order t, we can deduce that

$$\zeta_0 + (1-\psi)\,(\mathrm{d}\zeta_0/\mathrm{d}\psi) = A_0, \tag{S 4.21}$$

and

$$2\zeta_1 + (1-\psi)\,(\mathrm{d}\zeta_1/\mathrm{d}\psi) = A_1 - A_0\zeta_0/2 - A_0^3/12 + (2c-1)A_0\Xi_0/\sqrt{2}. \tag{S 4.22}$$

First, we integrate equation (S 4.21), to obtain

$$\zeta_0 = (1-\psi)\int_0^{\psi}\frac{A_0(\psi')}{(1-\psi')^2}\,\mathrm{d}\psi' = \frac{1-c\psi-(1-\psi)^c}{c(1-c)}, \tag{S 4.23}$$

which was obtained previously by equation (3.4). Then in equation (S 4.22), after applying the integrating factor $(1-\psi)^{-2}$, we obtain

$$\zeta_1(\psi) \approx (1-\psi)^2 \int_0^\psi \frac{1}{(1-\psi')^3} \left(A_1 - \frac{A_0\zeta_0}{2} - \frac{A_0^3}{12} + \frac{(2c-1)}{\sqrt{2}} A_0 \Xi_0 \right) \mathrm{d}\psi'. \tag{S 4.24}$$

Then, since A_0, ζ_0, Ξ_0, and A_1 depend solely on ψ (being given by equations (3.3), (3.4), (3.5) and (S 5.2), respectively), we obtain equation $\zeta_1 \equiv \zeta_1(\psi)$ which is given via equation (S 5.3) in section S 5.

(c) Correction at order t for upper region front horizontal location $\Xi(\psi, t)$

Having obtained an order t correction for $A(\psi, t)$ and $\zeta(\psi, t)$, we now compute the order t correction for Ξ, in the form $\Xi(\psi, t) \approx \Xi_0(\psi) + t\,\Xi_1(\psi)$. We first combine equations (2.6) and (2.7), and then, Taylor expanding $\tan(\alpha)$, we can obtain $\Xi \approx t^{-3/2} \int_y^1 \left(\alpha + \alpha^3/3\right)\, \mathrm{d}y$, where via equation (2.4), we substitute $\mathrm{d}y = -(t/2)\,\mathrm{d}\zeta$ at any given time t, and introducing similarity variable $\alpha = \sqrt{t/2}\,A$ given by equation (3.1), we deduce

$$\Xi \approx \frac{1}{2\sqrt{2}} \int_0^\zeta \left(A + t\,\frac{A^3}{6} \right) \mathrm{d}\zeta. \tag{S 4.25}$$

Then, introducing $A(\psi, t)$, which is given by equation (5.1), and using equation (5.2) to compute $\mathrm{d}\zeta \approx \mathrm{d}\zeta_0 + t\,\mathrm{d}\zeta_1$ (again at a given t), we express (S 4.25) in terms of ψ, as

$$\Xi \approx \frac{1}{2\sqrt{2}} \int_0^\psi A_0\,\frac{\mathrm{d}\zeta_0}{\mathrm{d}\psi}\,\mathrm{d}\psi + \frac{t}{2\sqrt{2}} \int_0^\psi \left(\left(A_1 + \frac{A_0^3}{6} \right) \frac{\mathrm{d}\zeta_0}{\mathrm{d}\psi} + A_0\,\frac{\mathrm{d}\zeta_1}{\mathrm{d}\psi} \right) \mathrm{d}\psi. \tag{S 4.26}$$

After integrating, we obtain $\Xi(\psi, t) \approx \Xi_0(\psi) + t\,\Xi_1(\psi)$, with $\Xi_1(\psi)$ as a well defined function in terms of ψ, which is given by equation (S 5.4) in section S 5. The functions A_1, ζ_1 and Ξ_1 are all plotted in Figure 1. Note, as commented earlier, they are all negative.

S 5. Form of equations $\Omega(\psi)$, $A_1(\psi)$, $\zeta_1(\psi)$, and $\Xi_1(\psi)$, in terms of parameter c

Here we solve equations (S 4.9), (S 4.15), (S 4.24) and (S 4.26), computed in section S 4 to determine $\Omega(\psi)$, $A_1(\psi)$, $\zeta_1(\psi)$, and $\Xi_1(\psi)$, respectively. The equations are solved in terms of ψ and c, as follows. As deduced before, equation (S 4.9) is expressed in terms of A_0, ζ_0 and Ξ_0, which are given by equations (3.3), (3.4) and (3.5), respectively, as well defined functions in terms of ψ. Hence, we can compute (S 4.9) as

$$\begin{aligned}\Omega(\psi) = (6c(2c-1)((2c-1)(1-\psi)^{2c} + (c+2)(1-\psi)^{c} - (c+1)(2c+1))\psi - (c+1)(2c-1)(2c+1)(1-\psi)^{3c} + \\ (-12c^3 - 30c^2 + 33c - 3)(1-\psi)^{2c} + (60c^3 + 60c^2 - 69c + 3)(1-\psi)^{c} - 44c^3 - 26c^2 + 35c - 1)/(48c^3(c^2-1)),\end{aligned} \tag{S 5.1}$$

where equations (3.3), (3.4) and (3.5) have reduced (S 4.9) to (S 5.1). Subsequently, we integrate equation (S 4.15), which depends on $\Omega(\psi)$, from which we deduce

$$\begin{aligned}A_1 = (((24c^4 - 24c^3 - 18c^2 + 24c - 6)(1-\psi)^{2c} + ((12c^5 + 18c^4 - 24c^3 - 18c^2 + 12c)\log(1-\psi) + 48c^5 - 12c^4 - 18c^3 + 48c^2 - 30c)(1-\psi)^{c} + 24c^5 \\ +24c^4 - 30c^3 - 30c^2 + 6c + 6)\psi + (2c^4 + 3c^3 - c^2 - 3c - 1)(1-\psi)^{3c} + (12c^4 + 66c^3 - 3c^2 - 48c + 9)(1-\psi)^{2c} + ((-12c^5 - 18c^4 + 24c^3 + 18c^2 \\ -12c)\log(1-\psi) + 54c^4 - 87c^3 - 87c^2 + 87c - 3)(1-\psi)^{c} - 68c^4 + 18c^3 + 91c^2 - 36c - 5)/(48c^7 - 96c^5 + 48c^3).\end{aligned} \tag{S 5.2}$$

Then, as equation (S 4.24) depends on A_0, ζ_0, Ξ_0 and A_1, which are given by equations (3.3), (3.4), (3.5) and (S 5.2), respectively, as well defined functions in terms of ψ and c, we can compute equation (S 4.24), as

$$\begin{aligned}\zeta_1(\psi) = (28 + 28c - 439c^2 + 710c^3 - 75c^4 - 564c^5 + 300c^6 + ((32c - 112c^2 + 56c^3 + 140c^4 - 112c^5 - 28c^6 + 24c^7)\log(1-\psi) - 324c^6 + 738c^5 - 204c^4 \\ -780c^3 + 744c^2 - 138c - 36)(1-\psi)^{c} + (36c^6 - 204c^5 + 267c^4 + 130c^3 - 317c^2 + 80c + 20)(1-\psi)^{2c} + (-12c^6 + 30c^5 + 12c^4 - 60c^3 + 12c^2 \\ +30c - 12)(1-\psi)^{3c} + ((16 - 112c + 220c^2 - 76c^3 - 188c^4 + 188c^5 - 48c^6)(1-\psi)^{2c} + (112c - 368c^2 + 436c^3 - 140c^4 - 272c^5 + 328c^6 \\ -96c^7 + (-24c^7 + 28c^6 + 112c^5 - 140c^4 - 56c^3 + 112c^2 - 32c)\log(1-\psi))(1-\psi)^{c} - 168c^7 + 112c^6 + 338c^5 - 232c^4 - 158c^3 + 148c^2 - 16)\psi \\ +(24c^8 + 8c^7 - 46c^6 - 17c^5 + 16c^4 + 3c^3)\psi^2)/(96c^{10} - 352c^9 + 192c^8 + 576c^7 - 672c^6 - 96c^5 + 384c^4 - 128c^3).\end{aligned} \tag{S 5.3}$$

Finally, integrating equation (S 4.26), which now depends on A_0, ζ_0, Ξ_0, A_1 and ζ_1, given by (3.3), (3.4), (3.5), (S 5.2) and (S 5.3), respectively, we find Ξ_1,

$$\begin{aligned}\Xi_1(\psi) = (&76 + 576c + 209c^2 - 4450c^3 - 2204c^4 + 12146c^5 + 4935c^6 - 15856c^7 - 2368c^8 + 6072c^9 + ((128c + 320c^2 - 1056c^3 - 2256c^4 + 2688c^5 + 4704c^6 \\ &-2144c^7 - 3344c^8 + 384c^9 + 576c^{10})\log(1-\psi) - 8352c^9 + 2784c^8 + 25208c^7 - 13000c^6 - 22756c^5 + 10948c^4 + 8732c^3 - 2060c^2 - 1392c - 112)(1-\psi)^c \\ &+((-128c - 256c^2 + 1152c^3 + 1632c^4 - 3192c^5 - 2856c^6 + 2648c^7 + 1768c^8 - 480c^9 - 288c^{10})\log(1-\psi) + 2304c^9 - 1776c^8 - 9896c^7 + 15056c^6 + 12714c^5 \\ &-15338c^4 - 5610c^3 + 3418c^2 + 1136c + 8)(1-\psi 2c + (-96c^9 + 1312c^8 + 968c^7 - 6712c^6 - 2716c^5 + 6204c^4 + 1604c^3 - 1396c^2 - 336c + 16)(1-\psi)^{3c} \\ &+(72c^9 + 48c^8 - 424c^7 - 279c^6 + 612c^5 + 390c^4 - 276c^3 - 171c^2 + 16c + 12)(1-\psi)^{4c} + ((-64 + 896c^2 - 496c^3 - 3212c^4 + 2732c^5 + 2924c^6 - 2764c^7 - 544c^8 \\ &+528c^9)(1-\psi)^{3c} + (64 - 192c - 1824c^2 + 384c^3 + 7124c^4 - 2340c^5 - 4676c^6 + 3828c^7 - 3856c^8 - 816c^9 + 1152c^{10} + (288c^{10} + 480c^9 - 1768c^8 - 2648c^7 \\ &+2856c^6 + 3192c^5 - 1632c^4 - 1152c^3 + 256c^2 + 128c)\log(1-\psi))(1-\psi)^{2c} + (64 + 512c + 1152c^2 - 1720c^3 - 7292c^4 + 4460c^5 + 13020c^6 - 13860c^7 \\ &-2912c^8 + 7728c^9 - 1152c^{10} + (-864c^{10} - 288c^9 + 4920c^8 + 1640c^7 - 6552c^6 - 2184c^5 + 2880c^4 + 960c^3 - 384c^2 - 128c)\log(1-\psi))(1-\psi)^c - 3456c^{10} \\ &-4176c^9 + 12360c^8 + 9160c^7 - 12448c^6 - 4912c^5 + 3976c^4 + 1832c^3 - 224c^2 - 320c - 64)\psi + ((-32c + 48c^2 + 360c^3 - 732c^4 - 696c^5 + 2292c^6 - 1000c^7 - 528c^8 \\ &+288c^9)(1-\psi)^{2c} + (-192c^2 - 268c^3 + 1396c^4 - 100c^5 - 3284c^6 + 4448c^7 + 784c^8 - 3360c^9 + 576c^{10} + (288c^{10} - 96c^9 - 1576c^8 + 504c^7 + 1848c^6 - 504c^5 \\ &-624c^4 + 96c^3 + 64c^2)\log(1-\psi))(1-\psi)^c + 576c^{11} + 1248c^{10} - 1328c^9 - 3404c^8 + 450c^7 + 2542c^6 - 70c^5 - 962c^4 - 92c^3 + 144c^2 + 32c)\psi^2)/(92^{17/2}c^{14} \\ &-152^{15/2}c^{13} - 592^{17/2}c^{12} + 952^{15/2}c^{11} + 72^{25/2}c^{10} - 1652^{15/2}c^9 - 872^{17/2}c^8 + 1052^{15/2}c^7 + 292^{17/2}c^6 - 52^{19/2}c^5 - 2^{21/2}c^4).\end{aligned} \tag{S 5.4}$$

We compute $A_1(\psi)$, $\zeta_1(\psi)$ and $\Xi_1(\psi)$, by fixing $c = 3/4$ (as per the main text) and using equations (S 5.2), (S 5.3) and (S 5.4), respectively. As can be seen in Figure 1, these variables become increasingly negative as ψ increases. This contrasts with the values of A_0, ζ_0 and Ξ_0 obtained in [1], all of which are positive.

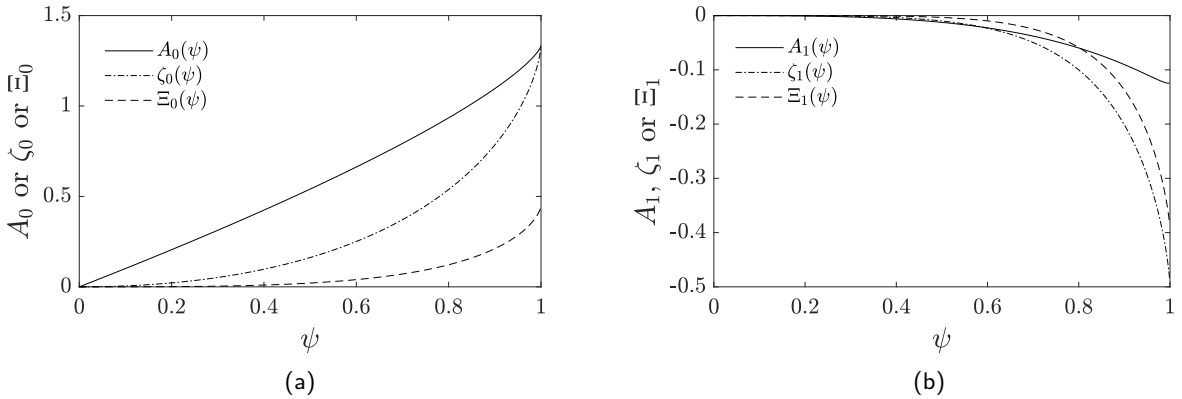

Figure 1: Functions appearing in first vs second order solutions. (a) A_0, ζ_0 and Ξ_0, computed by equations (3.3), (3.4) and (3.5) respectively, as given in the main text. Similar plots can be found in [1]. (b) $A_1(\psi)$, $\zeta_1(\psi)$ and $\Xi_1(\psi)$, computed by equations (S 5.2), (S 5.3) and (S 5.4), respectively.

In summary, the signs of $A_1(\psi)$, $\zeta_1(\psi)$ and $\Xi_1(\psi)$ indicate via equations (5.1)–(5.3) that, if the front shape is examined for a given ψ, the effect of having finite t is that film elements have rotated/reoriented less than the leading order formulae suggest. Likewise film elements are higher up vertically (higher y) and have fallen less far behind the leading edge (they have smaller ξ hence larger x) than the leading order formulae suggest.

S 6. Intersection between upper and lower region in terms of ψ for fixed $t_{\rm inj}$

Here we clarify how the upper region given at second order by equations (5.6) and (5.7), intersects with the lower region given also at second order by equation (5.8) (all these equations having been given in the main text). We require to find this intersection, in order to predict where the foam front has a concave corner for any given time t. We can track an injected material point in the upper region at different times t, by fixing an injection time $t_{\rm inj}$ and then varying $\psi \equiv 1 - t_{\rm inj}/t$ in equations (5.6)–(5.7) (upper region), and equation (5.8) (lower region). We then determine for which value of ψ both regions intersect. This is what we plot in Figure 2 for two values of $t_{\rm inj}$, i.e. $t_{\rm inj} \to 0$ and $t_{\rm inj} = 0.01$.

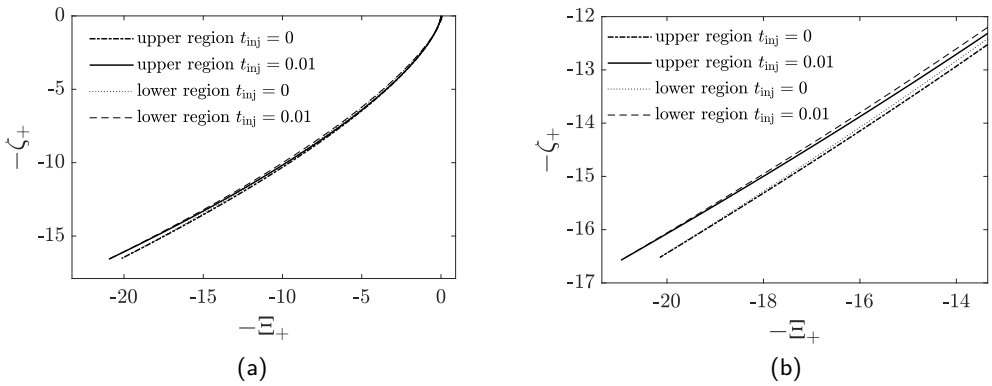

Figure 2: (a) Determining the matching point between the lower and the upper region of the front for two values of $t_{\rm inj}$. Here, $-\zeta_+$ and $-\Xi_+$ are the rescaled vertical y and horizontal x locations. By using equations (5.6) and (5.7) for the upper region, and equation (5.8), for the lower region, we found for a set of t values (obtained by varying ψ at fixed $t_{\rm inj}$), a particular ζ_+ value given by equation (5.6) at each ψ, with a corresponding Ξ_+ value given by either equation (5.7) or (5.8). When for a certain ψ, the Ξ_+ value coincides in both regions, the intersection occurs. Dash-dotted line: upper region at leading order with $t_{\rm inj} \to 0$. Solid line: upper region with $t_{\rm inj} = 0.01$. Dotted line: lower region formula with $t_{\rm inj} \to 0$. Dashed line: lower region formula for $t_{\rm inj} = 0.01$. For $t_{\rm inj} \to 0$, we found that the matching point occurs at $\psi_{\rm cross,0} \approx 0.9431$, with $\zeta_{+\rm cross,0} \approx 16.52$ and $\Xi_{+\rm cross,0} \approx 20.15$ (see the first order solution in section 4 of the main text). For $t_{\rm inj} = 0.01$, we found that $\psi_{\rm cross} \approx 0.9458$, obtaining that $\zeta_+(\psi_{\rm cross}) \approx 16.57$ and $\Xi_+(\psi_{\rm cross}) \approx 20.95$. (b) Inset zoomed view of (a) close to the cross over point.

Therefore, for a given time $t_{\rm inj}$, we compute $\zeta_+^{\rm upper}(\psi)$ (via equation (5.6)), and $\Xi_+^{\rm upper}(\psi)$ (via equation (5.7)) in the upper region. Then, for the specified $\zeta_+^{\rm upper}$, we set $\zeta_+^{\rm lower} = \zeta_+^{\rm upper}$, and compute $\Xi_+^{\rm lower}$ via equation (5.8). For fixed time $t_{\rm inj}$, we keep increasing ψ until the location of the upper region material point coincides with a material point in the lower region, so that $\Xi_+^{\rm upper} = \Xi_+^{\rm lower}$ (see also Figure 3). We denote the intersection point by $\zeta_{+\rm cross}$ and $\Xi_{+\rm cross}$ and it has a corresponding y value $y_{\rm cross}^{\rm inter}$ as can be obtained via equation (6.6) in the main text. Note that the ψ value corresponding to the intersection increases as $t_{\rm inj}$ increases (inset of Figure 3), at least for $t_{\rm inj}$ up to 0.01.

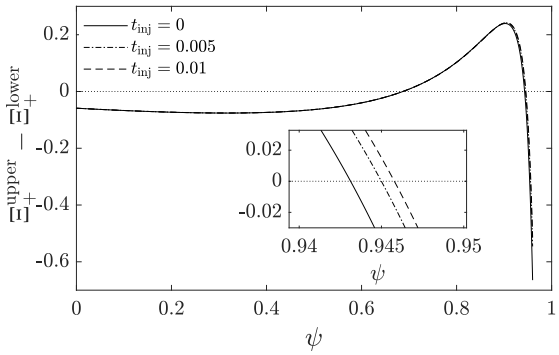

Figure 3: Front rescaled horizontal displacement difference between upper and lower region $\Xi_+^{\rm upper} - \Xi_+^{\rm lower}$, as a function of ψ. Here we see, for injected $t_{\rm inj}$, there are two values of ψ at which the upper and lower region intersect, the larger one being the correct value in each case. This verifies what is difficult to see on the scale of Figure 2(a), i.e. that there are two intersections, with the intersection we require, giving specifically a concave corner, being the one that is lower down in Figure 2(a), which corresponds here to the second intersection having the larger of the two ψ values. A zoomed view of the second intersection is shown here in the inset.

S 7. Perturbed location of the concave corner at time t

In section 6 in the main text we demonstrated that the value of orientation angle A_+ at the matching point, denoted $A_{+\rm cross}$ could be expanded in the form of equation (6.5), as

$$\begin{aligned} A_{+\rm cross} &\approx A_{+,0}(\psi_{\rm cross,0}) + t_{\rm inj}\left(\psi_{\rm cross,1}A'_{+,0}(\psi_{\rm cross,0}) + A_{+,1}(\psi_{\rm cross,0})\right) \\ &\equiv A_{+\rm cross,0} + t_{\rm inj}A_{+\rm cross,1}, \end{aligned} \tag{S 7.1}$$

where $A'_{+,0}$ denotes the function $\mathrm{d}A_{+,0}/\mathrm{d}\psi$ (which is obtained via equations (3.3) and (5.5) as given in the main text). Analogously, we can compute ζ_+ and Ξ_+ at the concave corner (denoted $\zeta_{+\rm cross}$ and $\Xi_{+\rm cross}$), via equations (5.6) and (5.7) (also given in the main text), as

$$\begin{aligned} \zeta_{+\rm cross} &\approx \zeta_{+,0}(\psi_{\rm cross,0}) + t_{\rm inj}\left(\psi_{\rm cross,1}\zeta'_{+,0}(\psi_{\rm cross,0}) + \zeta_{+,1}(\psi_{\rm cross,0})\right) \\ &\equiv \zeta_{+\rm cross,0} + t_{\rm inj}\zeta_{+\rm cross,1}, \end{aligned} \tag{S 7.2}$$

$$\begin{aligned} \Xi_{+\rm cross} &\approx \Xi_{+,0}(\psi_{\rm cross,0}) + t_{\rm inj}\left(\psi_{\rm cross,1}\Xi'_{+,0}(\psi_{\rm cross,0}) + \Xi_{+,1}(\psi_{\rm cross,0})\right) \\ &\equiv \Xi_{+\rm cross,0} + t_{\rm inj}\Xi_{+\rm cross,1}, \end{aligned} \tag{S 7.3}$$

where $\zeta'_{+,0}$ and $\Xi'_{+,0}$, denote the functions $\mathrm{d}\zeta_{+,0}/\mathrm{d}\psi$ and $\mathrm{d}\Xi_{+,0}/\mathrm{d}\psi$, respectively (obtained via equations (3.4), (3.5), (5.6) and (5.7), as given in the main text). We can also obtain analogous expressions in terms of t instead of $t_{\rm inj}$. Via equation (5.1) (given in the main text), the value A at the corner (denoted $A_{\rm cross}$), is given by (using also equation (6.1), as given in the main text)

$$A_{\rm cross} \approx A_0(\psi_{\rm cross,0} + t\,(1-\psi_{\rm cross,0})\psi_{\rm cross,1}) + t\,A_1(\psi_{\rm cross,0} + t\,(1-\psi_{\rm cross,0})\psi_{\rm cross,1}) \tag{S 7.4}$$

which upon expanding gives

$$\begin{aligned} A_{\rm cross} &\approx A_0(\psi_{\rm cross,0}) + t\,((1-\psi_{\rm cross,0})\psi_{\rm cross,1}A'_0(\psi_{\rm cross,0}) + A_1(\psi_{\rm cross,0})) \\ &\equiv A_{\rm cross,0} + t\,A_{\rm cross,1}, \end{aligned} \tag{S 7.5}$$

where A_0' denotes the function $\mathrm{d}A_0/\mathrm{d}\psi$ (obtained via equation (3.3)). Analogously, we can compute $\zeta \equiv \zeta_{\mathrm{cross}}$ and $\Xi \equiv \Xi_{\mathrm{cross}}$, via equations (5.2) and (5.3) (given in the main text), as

$$\begin{aligned}\zeta_{\mathrm{cross}} &\approx \zeta_0(\psi_{\mathrm{cross},0}) + t\left((1-\psi_{\mathrm{cross},0})\psi_{\mathrm{cross},1}\zeta_0'(\psi_{\mathrm{cross},0}) + \zeta_1(\psi_{\mathrm{cross},0})\right)\\ &\equiv \zeta_{\mathrm{cross},0} + t\,\zeta_{\mathrm{cross},1}, \end{aligned} \tag{S 7.6}$$

$$\begin{aligned}\Xi_{\mathrm{cross}} &\approx \Xi_0(\psi_{\mathrm{cross},0}) + t\left((1-\psi_{\mathrm{cross},0})\Xi_{\mathrm{cross},1}\Xi_0'(\psi_{\mathrm{cross},0}) + \Xi_1(\psi_{\mathrm{cross},0})\right)\\ &\equiv \Xi_{\mathrm{cross},0} + t\,\Xi_{\mathrm{cross},1}, \end{aligned} \tag{S 7.7}$$

where ζ_0' and Ξ_0', denote the functions $\mathrm{d}\zeta_0/\mathrm{d}\psi$ and $\mathrm{d}\Xi_0/\mathrm{d}\psi$, respectively (obtained via equations (3.4) and (3.5)). Predictions that arise from equations (S 7.1)–(S 7.3) and (S 7.5)–(S 7.7) are presented in section 7 of the main text.

A comparison between equations (S 7.1)–(S 7.3) and (S 7.5)–(S 7.7) can be made using equations (5.5)–(5.7) to identify the relationships between $A_{+,0}$, $\zeta_{+,0}$, $\Xi_{+,0}$, $A_{+,1}$, $\zeta_{+,1}$ and $\Xi_{+,1}$, and A_0, ζ_0, Ξ_0, A_1, ζ_1 and Ξ_1, noting also via (5.5)–(5.7) that

$$A_{+,0}' = \frac{A_0'}{(1-\psi)^{1/2}} + \frac{A_0}{2(1-\psi)^{3/2}}, \tag{S 7.8}$$

$$\zeta_{+,0}' = \frac{\zeta_0'}{(1-\psi)} + \frac{\zeta_0}{(1-\psi)^2}, \tag{S 7.9}$$

$$\Xi_{+,0}' = \frac{\Xi_0'}{(1-\psi)^{3/2}} + \frac{3\Xi_0}{2(1-\psi)^{5/2}}. \tag{S 7.10}$$

Equations (S 7.1)–(S 7.3) now become

$$\begin{aligned} A_{+\mathrm{cross}} &\approx \frac{A_0(\psi_{\mathrm{cross},0})}{(1-\psi_{\mathrm{cross},0})^{1/2}} \\ &\quad + t_{\mathrm{inj}}\left(\psi_{\mathrm{cross},1}\left(\frac{A_0'(\psi_{\mathrm{cross},0})}{(1-\psi_{\mathrm{cross},0})^{1/2}} + \frac{A_0(\psi_{\mathrm{cross},0})}{2(1-\psi_{\mathrm{cross},0})^{3/2}}\right) + \frac{A_1(\psi_{\mathrm{cross},0})}{(1-\psi_{\mathrm{cross},0})^{3/2}}\right), \end{aligned} \tag{S 7.11}$$

$$\begin{aligned} \zeta_{+\mathrm{cross}} &\approx \frac{\zeta_0(\psi_{\mathrm{cross},0})}{(1-\psi_{\mathrm{cross},0})} \\ &\quad + t_{\mathrm{inj}}\left(\psi_{\mathrm{cross},1}\left(\frac{\zeta_0'(\psi_{\mathrm{cross},0})}{(1-\psi_{\mathrm{cross},0})} + \frac{\zeta_0(\psi_{\mathrm{cross},0})}{(1-\psi_{\mathrm{cross},0})^2}\right) + \frac{\zeta_1(\psi_{\mathrm{cross},0})}{(1-\psi_{\mathrm{cross},0})^2}\right), \end{aligned} \tag{S 7.12}$$

$$\begin{aligned} \Xi_{+\mathrm{cross}} &\approx \frac{\Xi_0(\psi_{\mathrm{cross},0})}{(1-\psi_{\mathrm{cross},0})^{3/2}} \\ &\quad + t_{\mathrm{inj}}\left(\psi_{\mathrm{cross},1}\left(\frac{\Xi_0'(\psi_{\mathrm{cross},0})}{(1-\psi_{\mathrm{cross},0})^{3/2}} + \frac{3\Xi_0(\psi_{\mathrm{cross},0})}{2(1-\psi_{\mathrm{cross},0})^{5/2}}\right) + \frac{\Xi_1(\psi_{\mathrm{cross},0})}{(1-\psi_{\mathrm{cross},0})^{3/2}}\right), \end{aligned} \tag{S 7.13}$$

which are written in a form that can be readily contrasted with equations (S 7.5)–(S 7.7), with the various functions needed to evaluate all of these being specified in equations (3.3)–(3.5) and (S 5.2)–(S 5.4). The following relationships can now be derived (replacing terms in (S 7.8)–(S 7.10)

by counterparts from equations (S 7.5)–(S 7.7))

$$A_{+\mathrm{cross},0} = A_{\mathrm{cross},0}/(1-\psi_{\mathrm{cross},0})^{1/2}, \tag{S 7.14}$$

$$\zeta_{+\mathrm{cross},0} = \zeta_{\mathrm{cross},0}/(1-\psi_{\mathrm{cross},0}), \tag{S 7.15}$$

$$\Xi_{+\mathrm{cross},0} = \Xi_{\mathrm{cross},0}/(1-\psi_{\mathrm{cross},0})^{3/2}, \tag{S 7.16}$$

$$A_{+\mathrm{cross},1} = \frac{A_{\mathrm{cross},1}}{(1-\psi_{\mathrm{cross},0})^{3/2}} + \psi_{\mathrm{cross},1}\frac{A_{\mathrm{cross},0}}{2(1-\psi_{\mathrm{cross},0})^{3/2}}, \tag{S 7.17}$$

$$\zeta_{+\mathrm{cross},1} = \frac{\zeta_{\mathrm{cross},1}}{(1-\psi_{\mathrm{cross},0})^{2}} + \psi_{\mathrm{cross},1}\frac{\zeta_{\mathrm{cross},0}}{(1-\psi_{\mathrm{cross},0})^{2}}, \tag{S 7.18}$$

$$\Xi_{+\mathrm{cross},1} = \frac{\Xi_{\mathrm{cross},1}}{(1-\psi_{\mathrm{cross},0})^{5/2}} + \psi_{\mathrm{cross},1}\frac{3\Xi_{\mathrm{cross},0}}{2(1-\psi_{\mathrm{cross},0})^{5/2}}. \tag{S 7.19}$$

Consulting Table 1 in the main text, the terms $A_{+\mathrm{cross},1}$, $\zeta_{+\mathrm{cross},1}$, $\Xi_{+\mathrm{cross},1}$ turn out to have opposite sign from $A_{\mathrm{cross},1}$, $\zeta_{\mathrm{cross},1}$, $\Xi_{\mathrm{cross},1}$. It is clear from equations (S 7.17)–(S 7.19) that any sign changes must originate from the second term on each right hand side. In each expression, the origin of this second term is due ψ_{cross} increasing (by an amount $t_{\mathrm{inj}}\psi_{\mathrm{cross},1}$) to a value greater than $\psi_{\mathrm{cross},0}$ coupled to the tendency of $A_{+,0}$, $\zeta_{+,0}$ and $\Xi_{+,0}$ to increase with increasing ψ even without accounting for increases in A_0, ζ_0, Ξ_0 (due to the second term on the right hand side of equations (S 7.8)–(S 7.10)).

S 8. Tracking lower region material points to achieve matching

In the main text and also in section S 6 above, we used a procedure of second order accuracy in time to track the trajectory of an injected material point (injected at time t_{inj}) through the upper region in terms of ζ_+ and Ξ_+, as the rescaled y and x location. We followed its location over time until it coincided with the current location of a material point in the lower region, thereby allowing us to estimate the location of the concave corner. Once we know when and where the two regions coincide, we can figure out which material point in the lower region meets up with any given material point in the upper region. Then it is possible to track the trajectory of a lower region material point up to the matching point with the upper region material point labelled by t_{inj}: this is what Figure 4 in the main text achieves. In what follows we identify material points in the lower region by their original location on the front y_0 on the front at time $t=0$, and we explain how to find a relation between the lower region y_0 and the upper region t_{inj}, this relation then being used to produce the trajectories in Figure 4.

(a) Identifying the value of $\mathfrak{z}_0$

As we are interested in early-time solutions, and hence small values of t_{inj} and t, we expect that the material points of interest will be comparatively close to the top of the solution domain, hence y_0 values are expected to be close to unity. Accordingly (and in line with section S 3) we define $\mathfrak{z}_0 = 1-y_0$ as the vertical distance (measured down from the top of the solution domain) of a material point at its original location at time $t=0$. We anticipate that $\mathfrak{z}_0$ will be rather smaller than unity. In principle we can consider not only values $\mathfrak{z}_0>0$ (points already present on the front at $t=0$), but also $\mathfrak{z}_0<0$ (denoting a "virtual" material points not yet physically present on the front at time $t=0$, but which might be extracted from the concave corner later on [1]). Comparing equations (2.11) and (2.12) in the main text (and remembering that $5t^2/(48y_0)$ can be approximated by $5t^2/48$ when t is small and y_0 is close to unity), it follows that a lower region point released at

$t=0$ from $y=y_0$, follows a trajectory given by

$$y \approx y_0 - 1 + y_{2\mathrm{nd,lower}}(t) = -\mathfrak{z}_0 + y_{2\mathrm{nd,lower}}(t), \tag{S 8.1}$$

with the specific formula for $y_{2\mathrm{nd,lower}}(t)$ (the trajectory of a point initially at the top of the solution domain) given by equation (2.12) in the main text. If we suppose that the concave corner is at location $y_{2\mathrm{nd,cross}}(t)$ (see equation (6.7)) at any given time t, we can determine the $\mathfrak{z}_0$ value instantaneously at the corner via

$$\mathfrak{z}_0 \approx y_{2\mathrm{nd,lower}}(t) - y_{2\mathrm{nd,cross}}(t). \tag{S 8.2}$$

Here however we are interested in the first instance in obtaining $\mathfrak{z}_0$ as a function of t_{inj} rather than as a function of t. Within the expression for $y_{2\mathrm{nd,lower}}(t)$ (see equation (2.12)) it is a simple matter to replace t by $t_{\mathrm{inj}}/(1-\psi_{\mathrm{cross}}(t_{\mathrm{inj}}))$ where ψ_{cross} as a function of t_{inj} is obtained by the procedure outlined in section S 6. If we are specifically interested in the time at which the point $\mathfrak{z}_0$ reaches the concave corner tracked via the aforementioned procedure to a location $y=y^{\mathrm{inter}}_{\mathrm{cross}}(t_{\mathrm{inj}})$ at which upper and lower regions intersect, it now follows that

$$\mathfrak{z}_0 \approx y_{2\mathrm{nd,lower}}(t_{\mathrm{inj}}/(1-\psi_{\mathrm{cross}}(t_{\mathrm{inj}}))) - y^{\mathrm{inter}}_{\mathrm{cross}}(t_{\mathrm{inj}}). \tag{S 8.3}$$

Meanwhile employing equation (6.6) in the main text, $y^{\mathrm{inter}}_{\mathrm{cross}}$ can simply be written as $1-(t_{\mathrm{inj}}/2)\zeta_{+\mathrm{cross}}(t_{\mathrm{inj}})$ where again $\zeta_{+\mathrm{cross}}$ as a function of t_{inj} is obtained by the procedure outlined in section S 6. Hence

$$\mathfrak{z}_0 \approx -\frac{t_{\mathrm{inj}}}{2}\left(\frac{1}{(1-\psi_{\mathrm{cross}})} - \zeta_{+\mathrm{cross}}\right) + \frac{5t_{\mathrm{inj}}^2}{48(1-\psi_{\mathrm{cross}})^2}. \tag{S 8.4}$$

This has been plotted in Figure 4. This equation (S 8.4) can also be simplified in small t_{inj} limit by first recognising that $\zeta_{+\mathrm{cross}}=\zeta_{\mathrm{cross}}/(1-\psi_{\mathrm{cross}})$. Then ζ_{cross} is expanded as $\zeta_{\mathrm{cross},0}+t\,\zeta_{\mathrm{cross},1}$ (see equation (S 7.6)), with the factor t (which appears here within the perturbation term $t\,\zeta_{\mathrm{cross},1}$) approximated at leading order by $t_{\mathrm{inj}}/(1-\psi_{\mathrm{cross},0})$. In addition the factor $(1-\psi_{\mathrm{cross}})^{-1}$ in equation (S 8.4) can be approximated via

$$\frac{1}{(1-\psi_{\mathrm{cross}})} \approx \frac{1}{(1-\psi_{\mathrm{cross},0}-t_{\mathrm{inj}}\psi_{\mathrm{cross},1})} \approx \frac{1}{(1-\psi_{\mathrm{cross},0})} + \frac{t_{\mathrm{inj}}\psi_{\mathrm{cross},1}}{(1-\psi_{\mathrm{cross},0})^2}. \tag{S 8.5}$$

Retaining only terms out to order t_{inj}^2 within equation (S 8.4) gives

$$\mathfrak{z}_0 \approx -\frac{(1-\zeta_{\mathrm{cross},0})}{(1-\psi_{\mathrm{cross},0})}\frac{t_{\mathrm{inj}}}{2} + \left(\frac{5}{24} + \zeta_{\mathrm{cross},1} - (1-\zeta_{\mathrm{cross},0})\psi_{\mathrm{cross},1}\right)\frac{t_{\mathrm{inj}}^2}{2(1-\psi_{\mathrm{cross},0})^2}. \tag{S 8.6}$$

Inserting parameter values from Table 1 (as provided in the main text) now gives

$$\mathfrak{z}_0 \approx -0.530\,t_{\mathrm{inj}} + 1.845\,t_{\mathrm{inj}}^2. \tag{S 8.7}$$

Again this has been plotted in Figure 4. As can be seen in that figure, although equations (S 8.4) and (S 8.7) agree in the small t_{inj} limit, for larger t_{inj} they behave rather differently. Equation (S 8.7) predicts $\mathfrak{z}_0$ decreasing from zero reaching a minimum value of -0.0382 at $t_{\mathrm{inj}} \approx 0.144$ and returning to $\mathfrak{z}_0=0$ at $t_{\mathrm{inj}} \approx 0.288$. Negative $\mathfrak{z}_0$ values correspond to material points with $y_0>1$ that were not on the lower region of front originally but rather which have been extracted from the concave corner sometime after time $t=0$. The minimum (i.e. most negative) $\mathfrak{z}_0$ corresponds to the last extracted material point. After this, as $\mathfrak{z}_0$ begins to increase, the corner starts consuming previously extracted material points, and when $\mathfrak{z}_0=0$ all extracted points have now been consumed and the corner is beginning to consume points originally on the front $y_0 \le 1$. By contrast, equation (S 8.4) predicts a monotonically decreasing $\mathfrak{z}_0$, the magnitude of the derivative $|\mathrm{d}\mathfrak{z}_0/\mathrm{d}t_{\mathrm{inj}}|$ initially decreases with increasing t_{inj} but then an inflection occurs and $|\mathrm{d}\mathfrak{z}_0/\mathrm{d}t_{\mathrm{inj}}|$ increases again. The reason for this can be traced back to the behaviour of $\zeta_{+\mathrm{cross}}$ as predicted by the procedure of section S 6. For small t_{inj}, we find that $\zeta_{+\mathrm{cross}}$ is an increasing function of t_{inj}, but for larger t_{inj} the predicted value of $\zeta_{+\mathrm{cross}}$ decreases (see Figure 7(b) in the main text). The decrease in $\zeta_{+\mathrm{cross}}$ is what then drives equation (S 8.4) towards more negative $\mathfrak{z}_0$ values.

(b) Relating $\mathfrak{z}_0$ to the location of the concave corner

One of the issues we face with increasing $t_{\rm inj}$ is that the procedure in section S 6 for tracking an upper region material point up to the corner actually yields a poor estimate for the corner's location, at least when compared with a numerical Eulerian approach (see Figure 8 in the main text). In that case Figure 8 reveals that the function $y_{\rm 2nd,cross}(t)$ (equation (7.3)) actually gives a far better estimate of the location of the corner for any given t than a formula based on tracking material points through the upper region would. That suggests returning to equation (S 8.2) which gives $\mathfrak{z}_0$ directly as a function of t. To the extent that the formula (6.7) for $y_{\rm 2nd,cross}(t)$ is reliable, this enables us to identify which material point in the lower region is being extracted or consumed by the concave corner at any instant t, without even having to specify the corresponding material point in the upper region. Using the specific formulae for $y_{\rm 2nd,lower}(t)$ and $y_{\rm 2nd,cross}(t)$ from equations (2.12) and (7.3) in the main text, equation (S 8.2) predicts a minimum value of $\mathfrak{z}_0$ equal to -0.0114 at time $t \approx 0.759$ and predicts $\mathfrak{z}_0 = 0$ at time $t \approx 1.518$, i.e. the time at which $y_{\rm 2nd,lower} = y_{\rm 2nd,cross}$ as discussed in section 7(c) of the main text. To plot the resulting equation (S 8.2) on Figure 4 we need however to provide a relation between t and $t_{\rm inj}$. If we choose to approximate $\psi_{\rm cross} \approx \psi_{\rm cross,0} + t_{\rm inj}\psi_{\rm cross,1}$ as in equation (6.1) in the main text, we deduce

$$t \approx t_{\rm inj}/(1 - \psi_{\rm cross,0} - t_{\rm inj}\psi_{\rm cross,1}). \tag{S 8.8}$$

This is now inserted into equation (S 8.2). If we were to Taylor expand the resulting equation in powers of $t_{\rm inj}$, and discard all powers higher than order $t_{\rm inj}^2$, then equation (S 8.7) would result. Here however we do not carry out that formal expansion, retaining instead equations (S 8.2) and (S 8.8). The result is now plotted in Figure 4: qualitatively the shape is similar to equation S 8.7 but over a more compressed $t_{\rm inj}$ scale. Using the values for $\psi_{\rm cross,0}$ and $\psi_{\rm cross,1}$ reported in Table 1 in the main text, the time $t \approx 0.759$ giving the minimum $\mathfrak{z}_0$ is now considered to correspond to $t_{\rm inj} \approx 0.0320$. Meanwhile the time $t \approx 1.518$ at which $\mathfrak{z}_0 = 0$ corresponds to $t_{\rm inj} \approx 0.0508$.

(c) Tracking a particular material point in the lower region

When $t_{\rm inj}$ is sufficiently small, all the various methodologies discussed above to estimate $\mathfrak{z}_0$ give nearly the same prediction, so matching material points in the upper and lower region becomes straightforward again. Once we have identified, for any particular upper region material point $t_{\rm inj}$, the corresponding lower region material point $\mathfrak{z}_0$, we can track the vertical motion this material point executes via

$$y \approx 1 - \mathfrak{z}_0 - t/2 + 5t^2/48, \tag{S 8.9}$$

where equations (S 8.1) and (2.12) have been used, and all t values are considered up to the time at which intersection occurs between the specified upper and lower region material points. Equivalently defining $\zeta_+ = (1-y)/(t_{\rm inj}/2)$, $Z_0 = \mathfrak{z}_0/(t_{\rm inj}/2)$ and $\psi = 1 - t_{\rm inj}/t$ (now with $\psi \le \psi_{\rm cross}$), we deduce

$$\zeta_+ = Z_0 + \frac{1}{1-\psi} - t_{\rm inj}\frac{5}{24\,(1-\psi)^2}. \tag{S 8.10}$$

This then can be inserted into equation (5.8) to predict the ζ_+ vs Ξ_+ trajectory that the lower region material point executes as ψ and hence t varies. This is what we plot in Figure 4 in the main text for the cases $t_{\rm inj} \to 0$ and $t_{\rm inj} = 0.01$. The values of $\mathfrak{z}_0$ and hence $Z_0 \equiv \mathfrak{z}_0/(t_{\rm inj}/2)$ reported in Figure 4 in each instance have been obtained from equation (S 8.4). Note that as $t_{\rm inj} \to 0$, the value of $\mathfrak{z}_0 \to 0$ also, but Z_0 remains finite, turning out to have a value of $Z_0 \equiv \mathfrak{z}_0/(t_{\rm inj}/2) \approx -1.06$, as also follows from (S 8.7) in the $t_{\rm inj} \to 0$ limit.

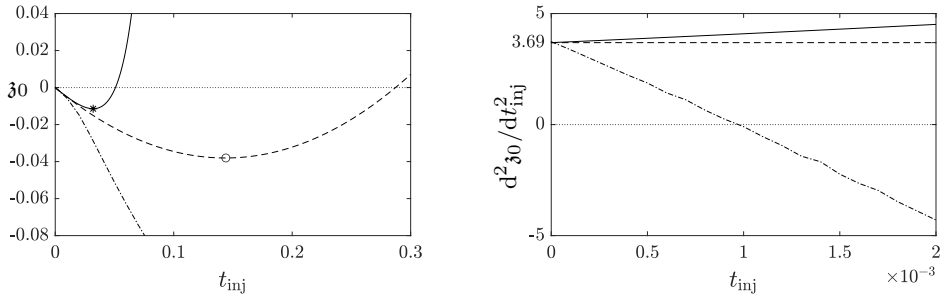

Figure 4: $\mathfrak{z}_0$ vs $t_{\rm inj}$ obtained via three different methodologies. Solid line: equations (S 8.2) (along with (S 8.8)). Dash-dotted line: equation (S 8.4). Dashed lined: equation (S 8.7). For small $t_{\rm inj} < 0.01$ values the three equations predict almost the same $\mathfrak{z}_0$ value, however the amount that they disagree increases as $t_{\rm inj}$ increases. In the case of equation (S 8.2), a minimum is found at $t_{\rm inj} \approx 0.0320$ (assuming (S 8.8) applies) the minimum value being $\mathfrak{z}_0 \approx -0.0114$ (point with asterisk "$*$" on the solid line). To the left of $*$, material points at the concave corner were not in the original solution domain of the lower region: they only appear when they are extracted from the concave corner. To the right of $*$, we start consuming material points again. At $t_{\rm inj} \approx 0.0508$, the value of $\mathfrak{z}_0$ reaches zero: all the extracted material points have been consumed. Hence for values of $\mathfrak{z}_0 > 0$ we start consuming material points that were originally on the front since time $t = 0$. Similarly, when the formula given by equation (S 8.7) is used, a minimum is found at $t_{\rm inj} \approx 0.114$ and $\mathfrak{z}_0 \approx -0.0382$ (point with "$\circ$" on the dashed line). This also predicts that at $t_{\rm inj} \approx 0.288$ all the extracted material points have been consumed ($\mathfrak{z}_0$ reaches zero here). In contrast, when equation (S 8.4) is used $\mathfrak{z}_0$ just becomes more negative as $t_{\rm inj}$ increases. (b) $\mathrm{d}^2\mathfrak{z}_0/\mathrm{d}t_{\rm inj}^2$ vs $t_{\rm inj}$ for $t_{\rm inj} < 0.002$. For equation (S 8.4) (dash-dotted line), this starts positive and then becomes negative for $t_{\rm inj} \sim 0.001$: this indicates an inflection for $\mathfrak{z}_0$ vs $t_{\rm inj}$ (albeit difficult to see on the scale of (a)). For equation (S 8.7) this corresponds to a constant $\mathrm{d}^2\mathfrak{z}_0/\mathrm{d}t_{\rm inj}^2$ value of 3.69. Finally for equation (S 8.2) (solid line), it starts positive and keeps increasing.

S 9. Front upper region extrapolation

Although equation (S 7.6) estimates $\zeta_{\rm cross}$ for any given t, it only approximates the nominal $\zeta_{\rm cross}$ value that would be computed via the intersection of equations (5.2), (5.3), and (5.4), as Figure 7(e) (in the main text) makes clear when comparing predictions. It may be necessary to extrapolate the solution of equations (5.2) and (5.3) over an interval of ζ from the vertical location where it intersects with equation (5.4) to an estimated $\zeta_{\rm cross}$ value by equation (S 7.6). As we saw in the main text, the estimated $\zeta_{\rm cross}$ obtained via (S 7.6) actually gives a better indication (see e.g. equation (6.7)) of how the vertical location of the concave corner evolves. Here we explain a simple way in which an extrapolation with respect to ζ can be achieved. We extrapolate the rescaled front's upper region shape $\zeta(\psi,t)$ vs $\Xi(\psi,t)$, and rescaled front orientation $A(\psi,t)$ vs $\zeta(\psi,t)$ at any given time t (as described by equations (5.1)–(5.3)), beyond the intercept between the upper (given by equation (5.2) and (5.3)) and the lower (given by equation (5.4)) region of the front, by considering a straight line extrapolation between the nominal $\zeta_{\rm cross}$ at the intercept itself and the estimate of $\zeta_{\rm cross}$ from equation (S 7.6). Specifically, we can expand equations (5.1)–(5.3), to obtain

$$A \approx A_0(\psi_{\rm cross,0}) + t\,A_1(\psi_{\rm cross,0}) + \chi\,t\,(1-\psi_{\rm cross,0})\psi_{\rm cross,1}A_0'(\psi_{\rm cross,0}), \tag{S 9.1}$$

$$\zeta \approx \zeta_0(\psi_{\rm cross,0}) + t\,\zeta_1(\psi_{\rm cross,0}) + \chi\,t\,(1-\psi_{\rm cross,0})\psi_{\rm cross,1}\zeta_0'(\psi_{\rm cross,0}), \tag{S 9.2}$$

$$\Xi \approx \Xi_0(\psi_{\rm cross,0}) + t\,\Xi_1(\psi_{\rm cross,0}) + \chi\,t\,(1-\psi_{\rm cross,0})\psi_{\rm cross,1}\Xi_0'(\psi_{\rm cross,0}). \tag{S 9.3}$$

Here, A_0', ζ_0' and Ξ_0', denote $\mathrm{d}A_0/\mathrm{d}\psi$, $\mathrm{d}\zeta_0/\mathrm{d}\psi$ and $\mathrm{d}\Xi_0/\mathrm{d}\psi$, respectively (with A_0, ζ_0 and Ξ_0 as given by equations (3.3)–(3.5)). Moreover, χ is a parameter that varies from 0 to unity, as ψ

varies from $\psi_{\mathrm{cross},0}$ to $\psi_{\mathrm{cross},0} + t_{\mathrm{inj}}\,\psi_{\mathrm{cross},1} \approx \psi_{\mathrm{cross},0} + t\,(1-\psi_{\mathrm{cross},0})\,\psi_{\mathrm{cross},1}$. We can obtain a straight line relation between A and ζ, and between Ξ and ζ as

$$A \approx \frac{A_0'(\psi_{\mathrm{cross},0})}{\zeta_0'(\psi_{\mathrm{cross},0})}\left(\zeta - \zeta_0(\psi_{\mathrm{cross},0}) - t\,\zeta_1(\psi_{\mathrm{cross},0})\right) + A_0(\psi_{\mathrm{cross},0}) + t\,A_1(\psi_{\mathrm{cross},0}), \qquad \text{(S 9.4)}$$

$$\Xi \approx \frac{\Xi_0'(\psi_{\mathrm{cross},0})}{\zeta_0'(\psi_{\mathrm{cross},0})}\left(\zeta - \zeta_0(\psi_{\mathrm{cross},0}) - t\,\zeta_1(\psi_{\mathrm{cross},0})\right) + \Xi_0(\psi_{\mathrm{cross},0}) + t\,\Xi_1(\psi_{\mathrm{cross},0}). \qquad \text{(S 9.5)}$$

Equations (S 9.4) and (S 9.5) are what we have plotted in Figure 9 (see main text for details) at fixed time $t=1$, with $\psi_{\mathrm{cross}} \approx 0.9003$, for values of ζ from the computed $\zeta(\psi_{\mathrm{cross}}) \approx 0.5839$ (i.e. the intersection between (5.2)–(5.3) and (5.4)) up to the prediction that equation (S 7.6) estimates namely $\zeta_{\mathrm{cross}} \approx 0.7711$.

References

1. P. Grassia, L. Lue, C. Torres-Ulloa, and S. Berres, "Foam front advance during improved oil recovery: Similarity solutions at early times near the top of the front," Journal of Fluid Mechanics, vol. 828, pp. 527–572, 2017.
https://doi.org/10.1017/jfm.2017.541.